Compaction-induced Anisotropy in Granular Materials: Effects of Grain Shapes on Fabric and Permeability Evolutions

JIKE LI

B.Eng (Hons)

THE UNIVERSITY OF
SYDNEY

Supervisor: A/Prof. Yixiang Gan
Associate Supervisor: Dr. Deheng Wei

A thesis submitted in fulfilment of
the requirements for the degree of
Master of Philosophy

School of Civil Engineering
Faculty of Engineering
The University of Sydney
Australia

18 February 2026

Statement of Originality

This is to certify that the content of this thesis is my own work. This thesis has not been submitted for any degree or other purposes.

I certify that the intellectual content of this thesis is the product of my own work and that all assistance received in preparing this thesis and sources have been acknowledged.

Jike Li

31/10/2025

Statement of AI Usage

During the preparation of the thesis, the author used Claude for spelling corrections, minor sentence restructuring, and clarity enhancement. The author confirms that where text was modified by generative AI, the content was reviewed for possible errors, inaccuracies, and bias. The author takes full responsibility for the submitted thesis, confirms the originality of the work, and has used generative AI in accordance with University guidelines and policies.

Abstract

Particle morphology plays a vital role in altering the mechanical and fabric evolution of granular materials due to compression. In general, increasing particle shape irregularity, quantified by higher values of fractal dimension and surface roughness, enhances the fabric anisotropy and contact strength of a granular assembly. Localised deformation occurs when it is more energetically favourable than distributed compression in granular materials. The localisation is observed as zones where particles break and pores collapse in many experiments. However, localised deformation does not necessarily involve particle breakage; the mechanism driven by the release from particle interlocking without fragmentation remains less investigated.

In this study, we reconstructed realistic irregular particles with controlled fractal dimension and surface roughness using Spherical Harmonics (SH). The particles are packed to resemble an oedometer test using the discrete element method (DEM). We measured anisotropic fabric and permeability in the virtual granular packings via fabric analysis and computational fluid dynamics (CFD).

To highlight the presence of localisation zones in the DEM models, we visualise the evolution of the strain rate and particle orientation fabric with respect to the loading strain. We also discussed possible mechanisms of compaction band formation associated with particle irregularity. In particular, the release from interlocking between rough particles sets the condition for localisation, and an increasing fractal dimension delays the band formation and speeds up the band propagation. From DEM simulations containing compaction bands, we take representative elementary volumes to evaluate the evolution of pore orientation fabric and permeability anisotropy. The most permeable direction aligns with the loading direction, and the permeability anisotropy shows a strong linear correlation with pore fabric anisotropy.

These findings establish that irregular particle morphology can drive deformation localisation without particle breakage, thereby influencing permeability anisotropy. In comparison with the indirect influence through pore alteration, the direct impact of particle morphology on permeability anisotropy is insignificant. This work provides microscopic insights into localised permeability evolution in deforming granular media, with implications for geotechnical and

hydrological applications where the anisotropic flow rate through deforming granular media is of interest.

Acknowledgements

This thesis would not have been possible without the guidance and support of many remarkable individuals. Firstly and most importantly, I would like to express my deepest gratitude to my supervisor, Dr Yixiang Gan, who provided the perfect balance of freedom to explore and to proceed. I would also like to thank Dr Deheng Wei for being my co-supervisor, whose intellectual rigour and unwavering patience shaped not only this research but also my development of confidence.

I am profoundly grateful to my panel members of progress evaluation meetings, Prof. David Airey and Dr François Guillard, who challenged my assumptions and pushed my research thinking to be both novel and realistic. Their questions about the limits of computational resources and suggestions for algorithmic alternatives motivate me to expand my academic reading.

My office colleagues created an environment where ideas could flow through honest critique and genuine collaboration. Yu Chen deserves special recognition for countless discussions and motivations, often over late-night chats. Si Suo provided valuable comments that resolved technical difficulties. Qingchen Liu provided technical and ethical support during the initiation of my study. The broader research group, including Zhang Shi, Mingrui Dong, Xu Wang, Haiyi Zhong, Dongsheng Chen, Xiaoqian Bi, Yingjie Gu, and Yuyao Zhang, fostered an intellectual community that is collaborative and relaxing.

Finally, my family sustained me through this journey in ways that transcend academic achievement. Despite financial pressure, my parents have paid all my fees and covered my living expenses in Sydney. My sister and friends reminded me that life exists beyond research. This accomplishment belongs to all of you as much as it does to me.

Contents

List of Figures

CHAPTER 1

Introduction

1.1 Background

Granular materials commonly present in natural and engineered systems, from soil and sediments to industrial powders and construction aggregates (Mitchell & Soga, 2005). Their mechanical and hydraulic behaviours are widely concerned in applications spanning geotechnical engineering, agriculture, and mineral processing. Granular materials exhibit directional properties that emerge from the shape and arrangement of discrete grains.

The particle shape influences the evolution of anisotropic mechanical (Oda et al., 1985; Cho et al., 2006; Fonseca, 2011; Yang & Luo, 2015; Wei et al., 2019; Nie et al., 2022; Chen et al., 2024) and hydraulic behaviours (Oda, 1985; Zhu et al., 1997; Zhu & Wong, 1999; Vajdova et al., 2004; Garcia et al., 2009; Kerimov et al., 2018; Wei et al., 2021; Zhao & O'Sullivan, 2022; Heap et al., 2024) in granular materials. The particle morphology, including angularity, sphericity, and surface roughness, governs contact mechanics, such as sliding resistance and rotational restraints. These contact mechanisms determine how particles interact and rearrange under loading, and collectively form macroscopic anisotropy in mechanical strength and hydraulic conductivity.

Multiscale approaches on various granular material systems demonstrate particle shape effects on anisotropic behaviours. For instance, laboratory studies using particles ranging from spherical glass beads to highly angular crushed aggregates have shown shape dependencies in the relationship between hydraulic conductivity and porosity (Mathavan & Viraraghavan, 1992; Li & Gu, 2005). Triaxial tests show that angular particles develop more distinct strength

anisotropy under identical loading conditions than round particles (Oda, 1982; Oda et al., 1985; Nie et al., 2022; Chen et al., 2024).

The degree of anisotropy at the micro scale is influenced by particle shape in relation to the contact formation, force transmission, and particle rearrangement during deformation (Chen et al., 2024). The discrete element method (DEM), pioneered by Cundall and Strack (1979), provides insights into these microscopic mechanisms. For instance, Chen et al. (2024) employed the multi-sphere technique to model particle assemblies using DEM, and numerically observed that angular particles amplify directional effect during loading through enhanced interlocking.

Compression-induced deformation localisation shows distinct particle rearrangement patterns from those due to distributed deformation or shear-induced localisation. Compaction bands have been observed across a range of porous rocks. Highly porous aeolian sandstones are widely present in geological reservoirs and aquifers. The Navajo formations in the western United States, for instance, contain structural discontinuities in the form of compaction bands characterised by collapsed pores (Mollema & Antonellini, 1996). Permeability within these bands is a few orders of magnitude lower than in the host rock (Olsson, 1999). In laboratory settings, discrete compaction bands have been reproduced in Bentheim sandstone, where intense comminution concentrated within narrow tabular zones perpendicular to the maximum compressive stress (Vajdova et al., 2004). Similar cataclastic compaction bands occur in high-permeability volcanic tuffs, where pore collapse during the localisation process suppresses the permeability; although localisation in initially low-permeability tuffs induces microcracks connecting adjacent pores and enhancing the permeability (Heap et al., 2024).

Analogous behaviour is observed in the processing of brittle granular materials. When compressed, cereal packs or snow develop oscillatory propagating compaction bands driven by consecutive grain breakage and pore collapse (Valdes et al., 2012; Barraclough et al., 2017). Blatny et al. (2022) investigated the origin of the propagation patterns using a material point method. In their simulation, compaction bands were reproduced through deformation of bars leading to pore closure. A range of compaction band propagation patterns emerged solely from elastoplastic constitutive behaviours and pore rearrangement without invoking breakage.

Similarly, compaction bands may occur in granular materials in the absence of particle breakage, such as within the soil under mat foundations. Where the soil is densely arranged, soil particles occupy a portion of the contact area between water and the foundation, blocking water-solid contact and resulting in a reduction in the buoyancy force. Reduced buoyancy is associated with lower porosity and permeability (Zhou et al., 2019). Overlooking the possible presence of low-permeability compaction bands may similarly lead to inaccuracies in estimating the buoyancy force acting on foundations.

The current study explores the possible occurrence of compaction bands in rigidly confined dense granular materials with particle breakage suppressed, while attempting to link the anisotropic fabric and hydraulic behaviour with particulate morphology during compaction processes. Figure 1.1 contains two schematic figures comparing the commonly investigated breakage-induced strain localisation with the shape-induced one characterised by local particle rotation in our scope.

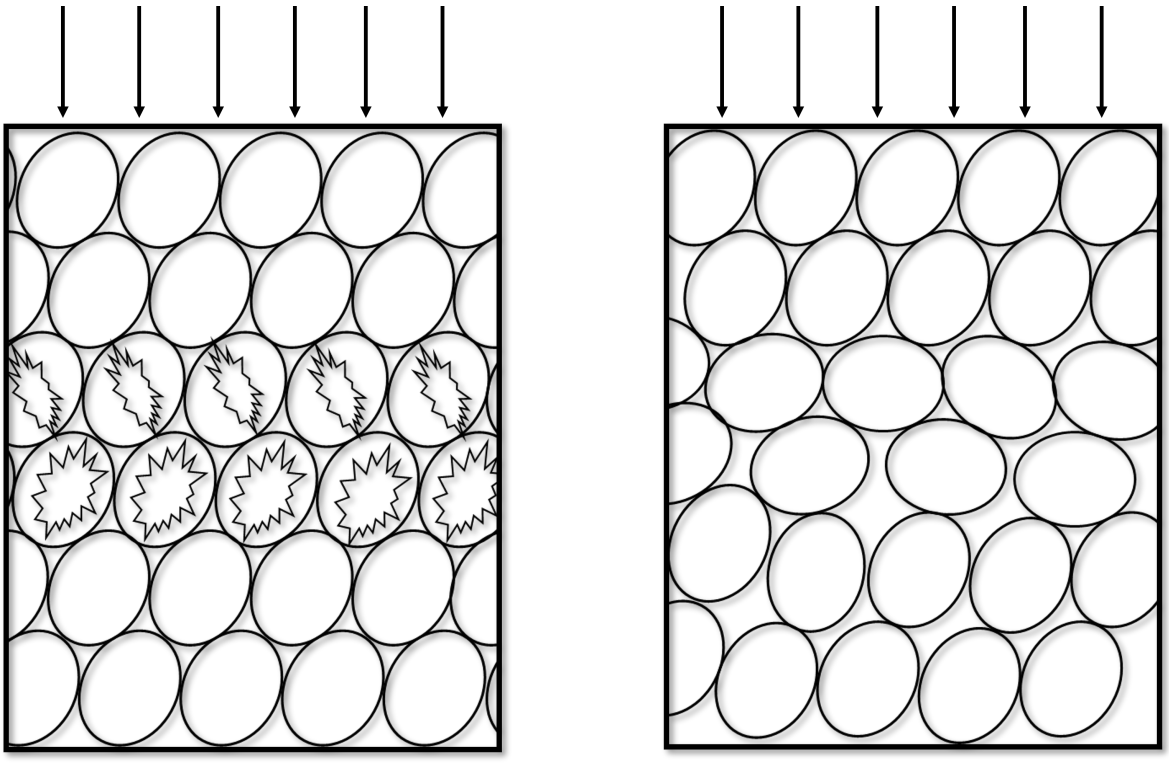

FIGURE 1.1: Schematic comparison of breakage-induced and the hypothesised shape-induced strain localisation mechanisms.

Within compaction bands, particle morphology plays a decisive role in controlling contact mechanics and force transmission, creating distinctive anisotropic patterns that differ from those observed in homogeneous deformation. Angular particles restrict reorganisation and

promote interlocking within these localised zones, while round grains facilitate rolling and more extensive rearrangement. These morphology-dependent behaviours generate unique fabric evolution patterns in compaction bands, directly influencing permeability anisotropy. Despite these mechanical insights, quantitative relationships between grain shape parameters, localised fabric evolution, and the resulting directional flow properties have not been systematically investigated.

This thesis addresses how particle morphology controls compaction band formation and the resulting evolution of fabric and permeability. Through numerical analyses of compaction bands using virtually reconstructed irregular particles, this research establishes quantitative relationships between particle shape, fabric tensor evolution, and permeability anisotropy within localised zones versus the unaffected matrix, providing insights into the micro-mechanical processes governing localised deformation.

1.2 Research objectives

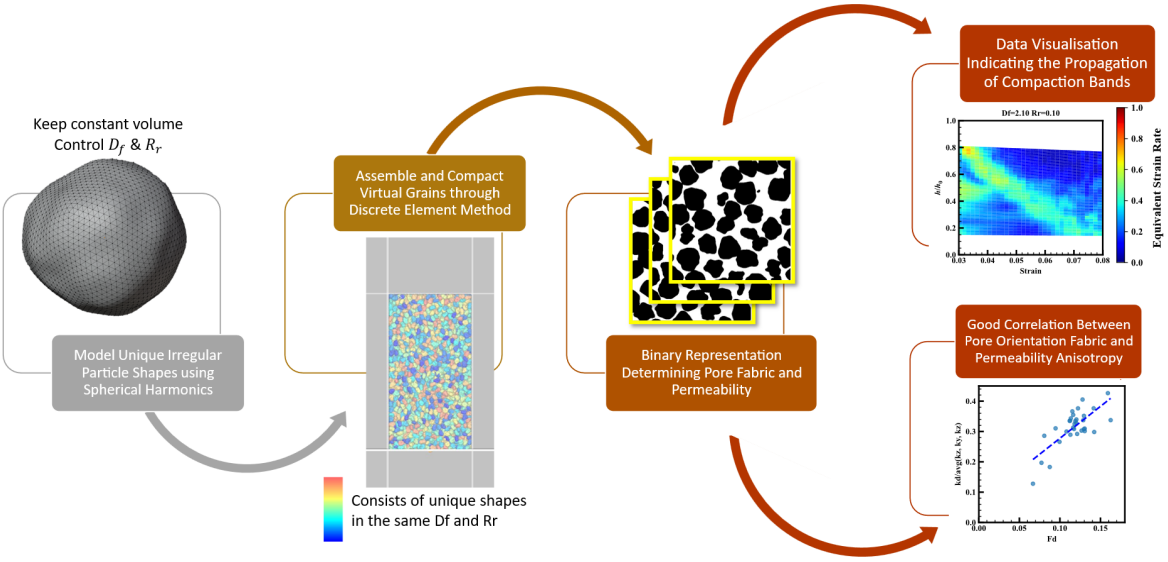

FIGURE 1.2: Graphical abstract of the integrated computational workflow, revealing shape-induced compaction band formation and correlation between pore-orientation fabric and permeability anisotropy.

The present research aims to advance understanding of how grain shapes affect fabric evolution and permeability in monodisperse granular sand using numerical methods. Specifically, it aims to obtain anisotropic granular structures from compaction bands and measure the evolution of

permeability during their development. Figure 1.2 represents the graphical abstract for this work. The key research objectives are:

- to investigate how particle morphology influences compaction band formation and propagation in dense granular materials in oedometer tests;
- to measure the fabric of particle orientation and void orientation in numerical models;
- to compute the permeability within regions of interest representing localised deformation or unaffected matrix in the models from multiple directions; and
- to characterise the relationship between the orientation fabric tensors and the permeability anisotropy.

1.3 Outline of the thesis

This thesis is organised into five chapters. This chapter, Chapter 1, provides an introduction to the thesis topic and a description of the research's main objectives.

Chapter 2 presents an overview of relevant works on the particulate nature or macroscopic properties of granular materials. The physical characterisation and the numerical modelling of particle sizes and shapes in granular materials are elaborated. The effect of inherent and induced fabric on the anisotropic soil behaviour of granular materials from nature or laboratories is demonstrated. The scalar and directional approaches of fabric quantification within the context of hydraulic conductivity are presented. Compaction band and shear band are two similar formations of localised deformation, and so they are compared through brief descriptions of their micro-structural mechanisms. Lastly, classical estimations of permeability incorporating the effect of particle sizes and shapes are illustrated.

Chapter 3 describes our approach to numerically study the effect of particle shape on the fabric and permeability anisotropy under loading. Virtual particles are reconstructed via Fourier transforms of spherical harmonics (SH), with angularity and surface roughness controlled by SH parameters. We selected SH parameters to include sphere, Leighton Buzzard sand (LBS), and a range of virtual irregular shapes. Then, DEM models representing an oedometer test are created using those reconstructed particles, initially aligned to amplify the effect of anisotropic fabric. The models are isotopically confined to a dense state and uniaxially compressed to

alter the fabric of both the solid phase and the pore space. Thereafter, we quantified the strain rate and particle orientation fabric to observe microscopic deformation patterns in DEM models. We also measured the alignment of pore space via pore orientation fabric and the permeability in three orthogonal directions. In this chapter, the methods for these procedures are described, and the validation of the DEM setup and permeability calculations is included.

In Chapter 4, the deformation patterns are presented through the evolution of the strain rate, porosity, and particle orientation fabric under vertical loading strain. Different formation and propagation patterns of strain localisation in the DEM simulations are evaluated in relation to the particle shape, and possible mechanisms are discussed. Moreover, pore-space measurements within representative elementary volumes from the DEM simulations are presented and discussed. The pore orientation fabric structurally characterises the pore-space anisotropy, and the hydraulic anisotropy is determined by the permeability along three orthogonal directions. The shape-dependence of the evolution of pore orientation fabric and the permeability anisotropy is elaborated.

Finally, Chapter 5 presents a summary of the work developed in this study, including key observations and recommendations for future work.

CHAPTER 2

Literature review

Sands are composed of discrete particles. The mechanical behaviour of sands is mainly determined by their particle characteristics (such as size and shape), particle arrangement, and inter-particle contacts. When sands are subjected to external loads, their particulate components will rearrange through translations and rotations, and potential particle breakage will induce small fragments to redistribute stresses in force chains. These will gradually alter the fabric (*i.e.*, the microstructural arrangement of particles) and the mechanical properties of the sand.

The mechanical properties of granular geomaterials are widely concerned in a wide range of applications and geological formations, including the injection and extraction of gas in depleted reservoirs for underground gas storage (Zhong et al., 2024), and the melt flow mechanism in partially molten regions of the upper mantle and lower crust (Bader et al., 2024). Therefore, it is essential to characterise the micro-scale properties of granular geomaterials, including particle characteristics and fabric, and their influence on permeability.

When subjected to external loads, geomaterials may exhibit irreversible deformation patterns. These include diffused compaction in the matrix and localised deformation in bands (Blatny et al., 2022). The latter, also called strain localisation, may occur as an inclined shear band or a planar compaction band. Strain localisation is represented by porosity reduction due to pore collapse or particle breakage, which is more drastic than that outside the band. In the context of hydraulic conductivity, strain localisation would alter the flow path (tortuosity) and may change the permeability (Zhu et al., 1997; Vajdova et al., 2004).

In this chapter, we review the relationships between particle characteristics, soil fabric, and hydraulic properties, with particular emphasis on compaction band formation and permeability

evolution. In Section 2.1, we cover the characterisation of particle size and morphology (shape). In Section 2.2, we demonstrate the definition and quantification of soil fabric (*i.e.*, particle arrangement). Then, in Section 2.3, we review the current theories about compaction bands, highlighting the formation mechanism and hydraulic behaviour. We also note that shear bands, another type of strain localisation, differ from compaction bands. We address how the permeability is influenced by soil fabric and compaction bands in Sections 2.2 and 2.3. We also include a separate section (Section 2.4) to elaborate on classical estimations of permeability in relation to particle size and shape.

2.1 Particle characterisation and modelling

The particle size and shape significantly influence the transport and mechanical behaviour of granular media (Kerimov et al., 2018). Notably, many authors use the term "morphology" to cover the overall particle shape and the fine surface features, as opposed to the term "form", which only concerns the overall shape. Extensive experimental and numerical evidence supports this importance, as reviewed in this section.

Numerical simulation has provided valuable insights into the microscopic mechanisms of granular materials. Cundall and Strack (1979) pioneered a method that explicitly calculates inter-particle contacts and particle motion, initially implementing spheres to simplify calculations. Subsequently, various 3D shapes have been introduced, including sphere clusters, bonded spheres, ellipsoids, super-ellipsoids, polyhedra, and numerous reconstructed irregular shapes. We also cover techniques for numerically reconstructing irregularly shaped particles.

2.1.1 Particle size

Particle size represents the most fundamental soil characterisation. Particle size gradation, reflected by the particle size distribution, serves as a primary determinant of soil type. Well-graded soils exhibit greater particle size variation compared to uniform soils and typically achieve lower void ratios, as smaller particles fill voids between larger particles (Miura et al., 1997). Particle size distribution also influences soil response: well-graded soils generally display larger friction angles (Holtz et al., 1981) and greater compressibility (Huffine &

Bonilla, 1962). Yamamuro and Wood (2004) demonstrated that small particles positioned between large grains can form unstable contacts, creating a more compressible soil skeleton in better-graded soils.

Multiple geometrical measurements exist for particle size, including sieve-determined grading, volume-equivalent diameter, and effective diameter. The particle size of soil has traditionally been characterised through sieving, which separates grains into size intervals. The particle size distribution is obtained by weighing the grain in each interval. Representative sizes can be calculated from this distribution, such as the median particle diameter d_{50}, which is defined as the sieve size that 50% of particles by weight pass through. Similarly, other sizes such as d_{60} and d_{10} can be extracted to calculate the coefficient of uniformity ($C_U = d_{60}/d_{10}$) (Mitchell & Soga, 2005) or estimate bulk material properties such as the permeability (Hazen, 1892, 1911). However, Taylor (2002) and Fernlund (1998) noted that this size definition remains ambiguous, with limited information available between sieve intervals. Moreover, standard laboratory sieving analyses are time-consuming and do not provide differentiation between grain forms.

Recent advances in scanning electron microscopy (SEM) and X-ray micro-tomography enable the acquisition of soil images where individual particles can be identified as groups of connected pixels or voxels. Two-dimensional (2D) images of individual particles may be processed digitally to extract the particle outline (Fonseca et al., 2009) (as depicted in Figure 2.1(a)), from which the unrolled diameter of the particle can be calculated. Based on image resolution (voxels per unit length) in three-dimensional (3D) images, particle volume and dimensions become readily available. The volume-equivalent diameter—the diameter of a sphere having equivalent volume to the particle—is commonly used as the particle size, such as in the Kozeny-Carman permeability equation (Kozeny, 1927). Al-Raoush (2007) also presented an effective diameter characterisation approach: $d_{\text{effective}} = \text{avg}(a, b, c)$, where $d_{\text{effective}}$ is the effective diameter, a, b, c represent the lengths of the particle's major, intermediate, and minor axes, and $\text{avg}()$ means the calculation of taking an average.

2.1.2 Particle shape

The particle shape is associated with many mechanical behaviours in granular materials. For instance, Guo and Su (2007) observed higher shear strength due to the particle interlocking caused by angularities in drained triaxial tests of irregular Ottawa sand. When subject to pressure differences, fluid flows through granular porous media. The ease of the fluid flow is dependent on the particle shape (Kozeny, 1927; Carman, 1939; Mathavan & Viraraghavan, 1992; Li & Gu, 2005; Wei et al., 2021). Thus, it is crucial to describe various shapes of soil particles.

Traditionally, particle shapes have been qualitatively described through visual inspection to classify soil as angular, sub-angular, rounded, or sub-rounded using standard charts (Fonseca, 2011). For example, Krumbein and Sloss (1963) developed a two-dimensional chart for visually comparing particles across a range of sphericity and roundness values based on binary particle images (see the chart in Figure 2.1(b)). And sphericity represents how closely a particle's form resembles a sphere, and roundness (or angularity) relates to the radius of the maximum inscribed circle at corners in 2D particle images (Wadell, 1932), as illustrated in Figure 2.1(c).

The widespread adoption of 2D image analysis techniques has facilitated the development of commercial software packages that measure particle shape from pixel-based images. Following image processing procedures, individual particles can be segmented and labelled, enabling the software to determine shape descriptors based on particle outlines (Fonseca, 2011). However, Fonseca (2011) pointed out a significant limitation: particles invariably rest in their most stable position when placed on a surface for imaging, restricting the viewing perspectives and the likely observed outline.

In light of the inherent limitation in capturing complete perspectives for precise shape characterisation and differentiation, 3D descriptions are employed. Many 3D shape descriptors are adopted from established 2D counterparts. Analogous to the 2D characterisation using pixels, 3D particle shape characterisations could also be formulated via voxel-based image data, which often consists of a series of 2D grey-scale or binary images.

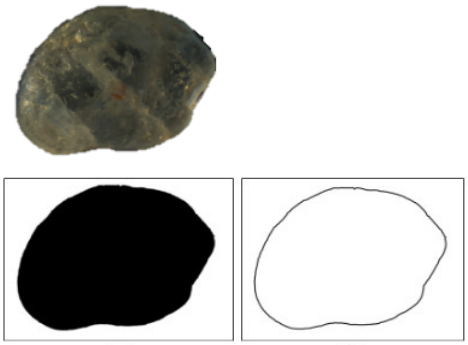

(a)

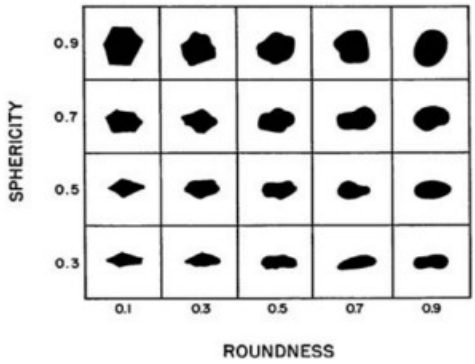

(b)

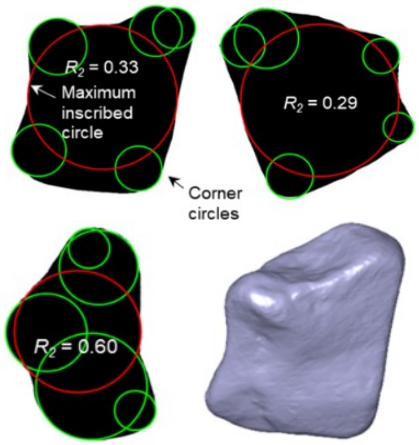

(c)

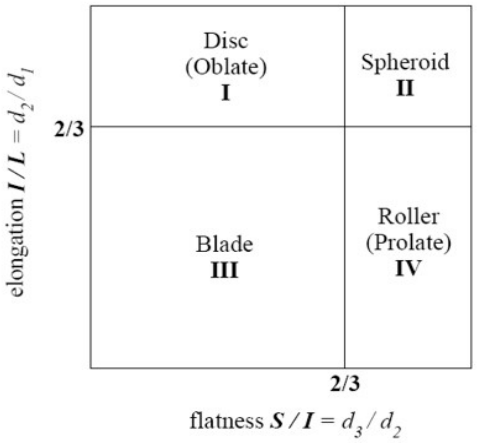

(d)

FIGURE 2.1: Two- and three-dimensional characterisations of the particle shape. (a) Outline detection of a sand grain for shape characterisation (adopted from Fonseca et al., 2009). From left to right: original image, binary image, and outline of the grain. (b) A chart for visually comparing particles across a range of sphericity and roundness values based on 2D binary images of particles (Krumbein & Sloss, 1963). (c) 2D measurements of the local roundness at the corners of a particle's projection images. Different local roundnesses are measured for the same particle due to different imaging angles (adopted from Zheng et al., 2021). (d) The classification of particle forms based on 3D aspect ratios (Zingg, 1935).

Aspect Ratio

A triaxial ellipsoid is an ellipsoid with three distinct semi-axes (or principal axis lengths) denoted as a, b, c ($a > b > c$), where the longest, medium, and shortest axes are the major, intermediate, and minor principal axes, respectively. The aspect ratio of a triaxial ellipsoid is given by the elongation ratio and the flatness ratio based on the three axis lengths:

$$\text{elongation} = b/a, \tag{2.1}$$

$$\text{flatness} = c/b. \tag{2.2}$$

Irregular particles also exhibit similar principal axes. Al-Raoush (2007) proposed a method to determine principal axis lengths via principal component analysis, which involves calculating the eigenvalues of the inertia matrix of each particle. Once the three lengths are obtained, the particle form can be classified as oblate, spheroid, blade, or prolate based on the values of the elongation ratio and the flatness ratio (Zingg, 1935), as shown by the diagram in Figure 2.1(d).

Sphericity

Sphericity describes how closely a particle resembles a sphere. Wadell (1932) defined it as $S_{\text{sphere}}/S_{\text{particle}}$, where S_{particle} is the surface area of the particle, and S_{sphere} is the surface area of the sphere in the same volume V_{particle}:

$$S_{\text{sphere}} = \sqrt[3]{36\pi V_{\text{particle}}^2}. \tag{2.3}$$

Thus, the sphericity S of a particle can be computed from its volume and surface area:

$$S = \frac{\sqrt[3]{36\pi V_{\text{particle}}^2}}{S_{\text{particle}}}. \tag{2.4}$$

Relative roughness

Relative roughness also measures how closely a particle resembles a sphere, but from a different perspective than sphericity. It quantifies the average irregularity of surface features as the global difference between the irregular particle surface and its volume-equivalent sphere (Wei et al., 2021). Within the spherical harmonics framework, surface roughness is represented through high-degree harmonic contributions. This approach effectively models roughness as small-scale form variations rather than a categorically distinct parameter. Taking a point i from the irregular particle surface, its distance from the particle centroid is r_i. Representing the irregular particle surface with n points, the relative roughness can be determined as:

$$R_r = \frac{\sqrt{\frac{1}{n}\sum_{i=1}^{n}(r_i - r_{\text{avg}})^2}}{r_{\text{avg}}}, \tag{2.5}$$

where n is a large integer and $r_{\text{avg}} = \sqrt[3]{\frac{3V_{\text{particle}}}{4\pi}}$.

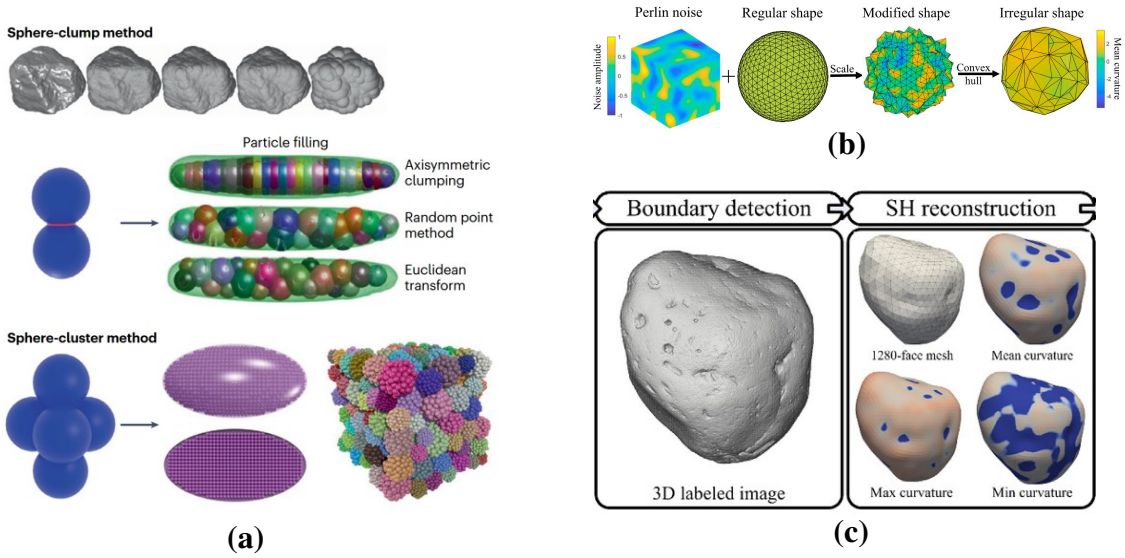

FIGURE 2.2: Modelling techniques for non-spherical particles. (a) The sphere-clump and sphere-cluster methods both model irregular particles using basic sphere elements. The difference is that the sphere-clump method allows overlaps (adopted from Zhao et al., 2023). (b) The generation process of an irregular convex particle from a scaled multiplication of the Perlin noise and the surface representation of a regular sphere (Kerimov et al., 2018). (c) An example of the reconstruction of real sand particles using spherical harmonics (SH) (Wei et al., 2019).

2.1.3 Modelling of realistic particles

The mechanical behaviour of granular materials fundamentally depends on the shape of the particles. Extensive experimental evidences demonstrate the strong influence of particle morphology on key mechanical properties, including compressibility, shear strength, dilation, and particle crushability (Guo & Su, 2007; Tsomokos & Georgiannou, 2010; Altuhafi & COOP, 2011; Yang & Luo, 2015). The discrete element method (DEM) has proven invaluable for understanding these particle shape effects, with accurate morphological representation being critical for model fidelity.

Initially implemented using circular particles (Cundall & Strack, 1979), DEM has evolved to capture the anti-rotation characteristics of irregular particles through rheology-type rolling resistance contact models applied to spherical particles (Iwashita & Oda, 2000; Jiang et al., 2005). A more direct alternative approach incorporates explicit irregular shapes in DEM simulations. For instance, Zhou et al. (2017) represents irregularly shaped particles in the ‘clump’ composed of overlapping particles (similar to Figure 2.2(a)). However, these

representations remain artificial and simplified, making them challenging to accurately and efficiently represent realistic particle morphology in the context of DEM simulations.

Kerimov et al. (2018) implemented 3D Perlin noise to generate irregular particles exhibiting randomness in morphology while allowing artificial elongations to control the aspect ratio and sphericity. Figure 2.2(b) presents the workflow briefly. This stochastic approach provides computational efficiency for creating large populations of statistically similar particles. However, they don't represent the fine morphology features of real particles.

The development of X-ray micro-computed tomography has provided a powerful tool for obtaining a precise 3D representation of grains, with the iso-surface at the solid-pore interface representing the surface of each particle. A simple method for reconstructing the particle surface is to use an image processing technique called the marching cubes algorithm, which can extract a polygonal mesh of an iso-surface from 3D scalar voxels (Cline et al., 1987; Lindblad, 2005). However, surfaces generated through marching cubes exhibit artificial stair-step artefacts that cause inaccurate measurements of shape parameters, such as surface area and local roundness, and may pose difficulties in clump generation within the DEM framework.

To overcome the issues of marching cubes, a more sophisticated method using spherical harmonics (SH) has been developed to reconstruct 3D particle surfaces (Zhou & Wang, 2015; Wei et al., 2018). The spatial Fourier transform of spherical harmonics can model any particle shape while preserving fine morphological features through the frequency decomposition of the particle surface. The method captures the overall form and fine morphology features across multiple length scales, as depicted in Figure 2.2(c).

Spherical harmonics can be formulated in either Cartesian or polar coordinate systems (Wei, 2021). As in Eq. (2.6), any spherical scalar function can be decomposed as the sum of spherical harmonics (SHs):

$$f(\theta,\varphi)=\sum_{n=0}^{\infty}\sum_{m=-n}^{n}c_n^m Y_n^m(\theta,\varphi), \tag{2.6}$$

where $Y_n^m(\theta,\varphi)$ and c_n^m are the spherical harmonic and coefficient at degree n and order m (Press et al., 1992), $\theta \in [0,\pi]$ and $\varphi \in [0,2\pi)$ denoting latitudinal and longitudinal

coordinates. Spherical harmonics reconstruct the surface of a real particle by fitting discretised surface points, which can be represented as $r_i(\theta, \varphi)$ in polar coordinates or as $\mathbf{v}_i(x_i(\theta, \varphi), y_i(\theta, \varphi), z_i(\theta, \varphi))$ in Cartesian coordinates, where i denotes the i-th point.

Wei (2021) compared polar-SH and Cartesian-SH methods in finite discrete element studies of particle breakage, demonstrating that both approaches generate higher quality surface meshes than commercial generalised marching cubes algorithms. However, each approach exhibits distinct limitations: polar-SH reconstructions may produce unrealistic surface features such as bumps and protrusions, particularly for highly irregular particles where the single-valued radius assumption breaks down. Conversely, Cartesian-SH implementations can introduce mesh distortions arising from surface parametrisation challenges when mapping complex 3D geometries onto regular grids.

2.2 Soil fabric characterisation

The mechanical and hydraulic responses of granular materials are intrinsically linked to their internal structure, commonly termed fabric. Fabric is defined as the arrangement of particles, particle groups, and pore spaces within the soil. And fabric is determined by particle morphologies, relative particle positions, and their contacts. Quantification of the fabric involves examining various entities such as particle orientations, contact normal orientations, branch vector orientations, and void orientations.

2.2.1 Fabric quantification

The primary sources of anisotropy are related to the particle shape, the pore geometry, and the contact normal orientation in a granulate system (Oda et al., 1985). Quantifying the fabric in a granular assembly requires obtaining data on the spatial distribution of particles and pore spaces within the material. Relevant studies are usually conducted experimentally using opaque soils or numerically through the DEM. In experiments , optical microscopic techniques have been used to provide images for fabric characterisation, including thin sections (Oda, 1972a) and scanning electron microscopy (Wang et al., 2020); it is also possible to obtain 3D images of the internal structure either via non-invasive techniques such as X-ray Computed

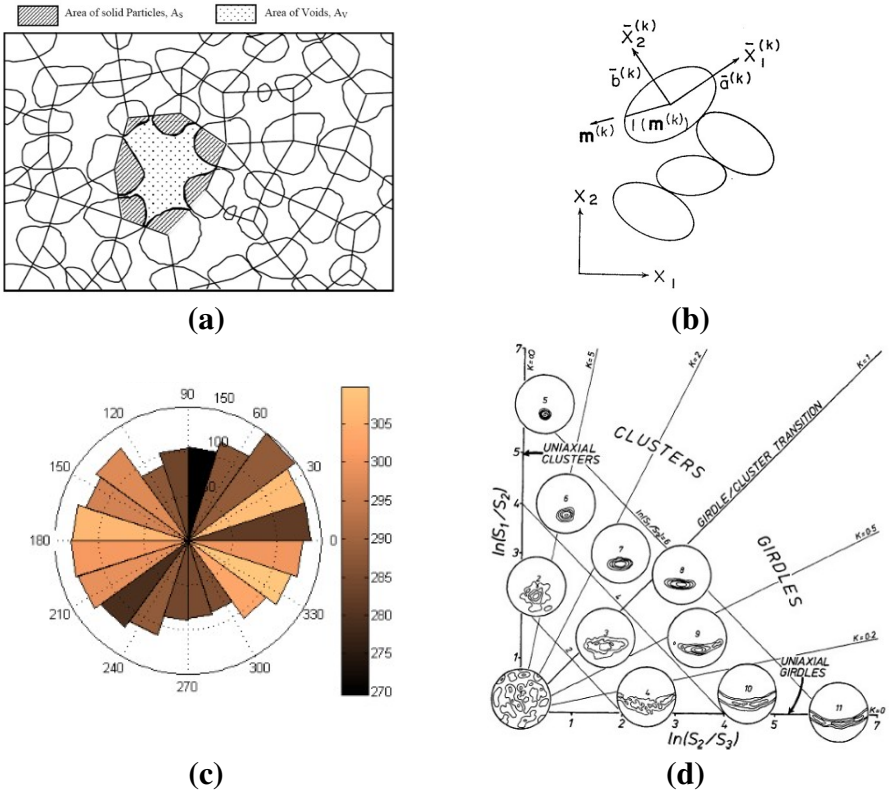

FIGURE 2.3: Quantification of soil fabric. (a) The local porosity, as a scalar fabric quantity, can be calculated geometrically in local regions formed by connecting the centroid of particles (adopted from Yang, 2005). (b) The orientation of a non-spherical geometry inclining relative to the coordinate axes (Oda et al., 1985). (c) A rose diagram of the polar angle distribution of void orientation from a sample (Fonseca, 2011). (d) Orientation data can be characterised by the ratios between three eigenvalues S_1, S_2, and S_3 from the principal component analysis (Woodcock, 1977).

Tomography (CT) (Bader et al., 2024) and Magnetic Resonance Imaging (MRI) (Iwashita & Oda, 2020), or invasive techniques by serial sectioning (Yang, 2005) or X-ray CT scanning of resin-impregnated samples (Nguyen et al., 2014). In contrast to the rigorous process of data acquisition from experiments, the spatial distribution of pores, particles, and contacts is digitally available from numerical models. The fabric could be quantified as average scalar quantities or statistical directional data from the obtained spatial distributions.

Scalar quantity

The void ratio is the most basic fabric measurement that quantifies the packing density of a material. The void ratio (e) is defined as the ratio between the volume of voids (V_v) and the volume of solid particles (V_s):

$$e = \frac{V_v}{V_s}. \tag{2.7}$$

It is common to present the void ratio of a whole sample in a single value. However, the spatial distribution of the void ratio can also be obtained by dividing the image into multiple sections using moving windows (Chork et al., 1994) or dividing the image into polygons based on the centroid of particles (such as Kuo et al., 1998; Yang, 2005; Fu and Dafalias, 2015). Figure 2.3(a) schematically presents the polygon-based method, where the local porosity can be calculated from the area of solid particles A_S and voids A_V. The distribution map of the void ratio can be used to indicate inherent heterogeneity or deformation-induced strain localisation.

Statistical analysis of directional data

The fabric also includes directional data, such as the orientation of the particles or the voids. Figure 2.3(b) shows the orientation of a non-spherical geometry in 2D, where $\bar{x_1}$ indicates the major orientation. In a 3D space, a direction may be quantified by its azimuth angle θ ($0 \leq \theta \leq 2\pi$) and polar angle ϕ ($0 \leq \phi \leq \pi$) in a spherical coordinate system. The directional data may be analysed statistically using histograms or visualised spatially via rose diagrams. For instance, Figure 2.3(c) presents a rose diagram of the polar angle distribution of void orientation from a granular sample (Fonseca, 2011).

In the context of soil mechanics, the fabric tensor is commonly computed to represent the average spatial orientation of particles or voids. Satake (1982) wrote the fabric tensor Φ in its simple form of a second-order symmetric tensor as:

$$\Phi_{ij} = \frac{1}{N} \sum_{k=1}^{N} n_i^k n_j^k, \tag{2.8}$$

where N is the total number of particles and n_i^k is the unit orientation vector. The fabric tensor could also incorporate particle sizes and shapes through weighted calculation (Oda et al., 1985):

$$\Phi_{ij}^{\text{particle}} = \frac{1}{\lambda} \sum_{k=1}^{N_p} Q_{ki}^p Q_{lj}^p S_{kl}^p, \tag{2.9}$$

where N_p is the number of particles, and λ ($= \sum_{p=1}^{N_p} (a^p + b^p + c^p)$) is an average measure of the major, intermediate, and minor half lengths (a^p, b^p, and c^p) of the particles; for each particle,

Q_{ki} and Q_{lj} are the rotational tensor, and S_{kl} is a tensor representing particle dimensions:

$$S_{kl}^{p} = \begin{bmatrix} a^{p} & 0 & 0 \\ 0 & b^{p} & 0 \\ 0 & 0 & c^{p} \end{bmatrix}. \tag{2.10}$$

The fabric tensor can be decomposed into eigenvalues to obtain the principal fabric parameters (O'Sullivan, 2011). The eigenvectors of the fabric tensor give the dominant orientation of fabric anisotropy, and the eigenvalues ($\Phi_1 > \Phi_2 > \Phi_3$) indicate the magnitude of preference in each direction. The major preferential orientation is related to the eigenvector corresponding to the highest eigenvalue.

The fabric anisotropy has been formulated between the eigenvalues. For instance, Thornton (2000) adopted the difference $\Phi_1 - \Phi_3$ and Zhao and Zhou (2017) implemented the ratio Φ_1/Φ_3 to represent the degree of anisotropy, where higher values are associated with greater anisotropy. Woodcock (1977) proposed a graphical interpretation of orientation fabric data using ratios between the three eigenvalues, as shown in Figure 2.3(d); based on this, Kuo et al. (1998) and Barreto et al. (2009) used a definition of deviator fabric:

$$\Phi_d = \frac{1}{\sqrt{2}}\sqrt{(\Phi_1 - \Phi_2)^2 + (\Phi_2 - \Phi_3)^2 + (\Phi_3 - \Phi_1)^2}. \tag{2.11}$$

2.2.2 The role of fabric

The strength, stiffness, and permeability of granular soils can be anisotropic depending on the inherent and induced anisotropy (Casagrande, 1944). The intrinsic anisotropy is the result of the depositional process (Oda, 1972a), and the induced anisotropy is associated with contact redistribution due to stresses applied to and strains induced in the soil (Oda, 1972b; Druckrey et al., 2016). Anisotropic fabrics are reassembled by anisotropic deposition of particles, forming directional force chains and connected pore structures, subsequently leading to the anisotropy in the mechanical response (Oda, 1977) and the hydraulic behaviour (Oda, 1985).

Particle morphology (shape) is considered fundamental to fabric and greatly influences the macroscopic behaviour of granular soils. The particle shape is often characterised at three length scales - overall angularity, local roundness, and surface roughness. Recent

experimental and numerical studies have revealed the mechanism by which particle shape affects the strength, stiffness, and permeability through the fabric.

The constitutive behaviour of sands is affected by the particle morphology and the internal fabric. Chen et al. (2024) numerically investigated the effect of the overall regularity and the surface roughness on the contact behaviour of particles in drained triaxial compression tests. They observed that the decreasing regularity is associated with a higher coordination number, but the increasing surface roughness tends to enhance the internal structure and particle orientation fabric anisotropy. Cabalar and Hasan (2013) conducted oedometer tests on sand-clay mixtures, where finer clay stays in the pores between host sand particles. The experiments show that a host sand with particle shapes different from spherical can contribute differently to the compressibility of the sand-clay mixture.

Experimental evidence confirms the relevance of stiffness and fabric in granular materials. Stiffness anisotropy, indicated by direction-dependent measurements of shear wave velocities, has been observed in freshly formed samples under an isotropic loading condition (Fonseca, 2011) due to the interlocking between particles.

Permeability, the ease with which fluid can travel through a porous medium, is governed by the interconnected pore structure, which can be characterised by the porosity and the void orientation fabric. The geometry of the solid matrix controls the shape and connectivity of the pore space, thereby controlling the permeability. Kerimov et al. (2018) simulated fluid flow through granular porous materials consisting of irregularly shaped particles, and found that higher angularity is associated with less permeability.

Fabric evolution due to loading, particularly anisotropic deformation, strongly affects permeability. Zhu et al. (1997) observed a significant decrease in porosity and permeability due to grain crushing and pore collapse in porous sandstones undergoing shear-enhanced compaction. During compaction, microcracks form preferentially along the direction of loading, allowing easier fluid flow in that direction and leading to permeability anisotropy. Localised deformation also contributes to spatial differences in the porosity and fabric, thereby causing heterogeneity in the magnitude and anisotropy of permeability (Vajdova et al., 2004).

The relationship between stress-induced fabric anisotropy and the resulting evolution of hydraulic permeability in granular media remains contested. The evolution of mechanical

fabric is well-documented and consistently observed to align with the major principal stress direction. The corresponding evolution of hydraulic anisotropy is less understood, partly because existing approaches to link fabric measures with permeability prediction remain limited.

Kuhn et al. (2015) adopted Discrete Element Method (DEM) and Lattice Boltzmann Method (LBM) to directly simulate fluid flow within the pore space. They identified correlations between void fabric measures and permeability evolution, particularly the median radial breadth tensor $\mathbf{R}^v$, which reflects directional hydraulic radius. However, their study stopped short of proposing a predictive constitutive relationship. Moreover, their chosen measure for void shape anisotropy—the Minkowski tensor $W_3^{v,2,0}$—exhibited erratic progression and high sensitivity to subtle particle rearrangements, limiting its utility as a fabric descriptor for permeability modelling.

Morimoto et al. (2024) attempted a more direct link by proposing a tensor-based permeability model derived from Effective Medium Theory. Their formulation predicts the permeability tensor from local throat conductances and orientations. However, this approach embeds a circularity: local conductance is defined as inversely proportional to throat length, so axial compression mathematically shortens throat lengths in the loading direction and forces the model to predict increased conductance there. The resulting alignment between permeability anisotropy and pore geometry is an artifact of the geometric input assumptions rather than an emergent hydrodynamic result.

2.3 Compaction band

Compaction bands are planar zones of strain localisation often characterised by compactive cataclasis with negligible shear (Mollema & Antonellini, 1996). Strain localisation represents local porosity reduction in granular materials (Vajdova et al., 2004). And these planar zones are oriented sub-perpendicular to the maximum principal stress (Baud et al., 2004).

Compaction bands and shear bands are two fundamentally different types of strain localisation. Their general features, including the orientation, mechanical responses, and hydraulic effects,

are compared herein. As depicted in Figure 2.4(a) and (b), compaction bands orient sub-perpendicular to the maximum principal stress, and shear bands form an inclined angle with the load. Compaction bands are dominated by negative volumetric strain with negligible shear offset, and shear bands are related to the onset of dilatancy (Zhu et al., 1997). Compaction bands are primarily associated with shear-enhanced compaction, leading to strain hardening and macroscopically ductile failure (Issen & Rudnicki, 2001; Heap et al., 2024), and shear bands are associated with strain softening and brittle failure (Heap et al., 2024). Compaction bands act as hydraulic barriers and cause significant permeability reduction (Vajdova et al., 2004). Although shear bands play a similar role in highly porous rocks by decreasing permeability due to pore collapse, they generally increase permeability in low-porosity rocks due to microcracks (Zhu et al., 1997; Vajdova et al., 2004).

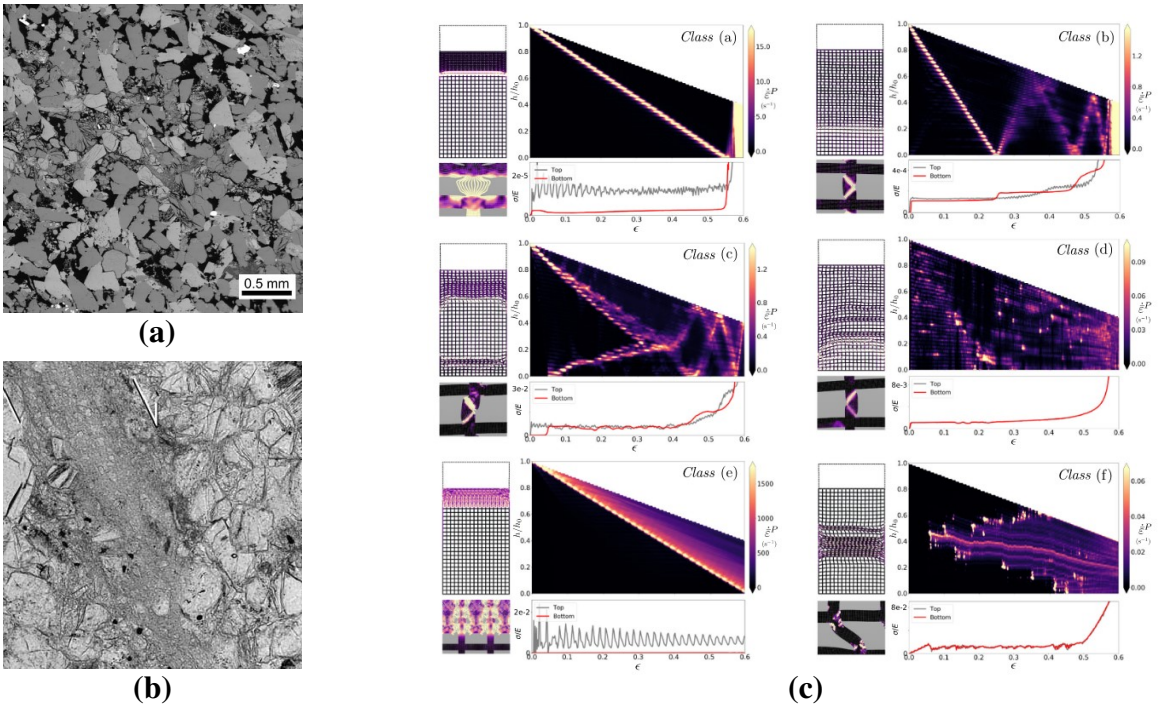

FIGURE 2.4: Macroscopic patterns of strain localisation. (a) A scanning electron microscopy (SEM) image of the compaction band, characterised by a lateral zone of low porosity (adopted from Heap et al., 2024). (b) An SEM image of the shear band at an inclined angle (Vajdova et al., 2004). (c) Different patterns of compaction band propagation and oscillation due to different loading rates and yield strengths. The propagation of compaction bands is visualised via strain rates in colour (Blatny et al., 2022).

2.3.1 Micro-structural mechanisms of compaction bands

Compaction bands usually occur in the process of shear-enhanced compaction or cataclastic flow, which leads to strain hardening and ductile failure, characterised by the irreversible plastic strains due to compactive pore collapses (Zhu et al., 1997). Compaction bands are primarily attributed to grain crushing and comminution in granular materials. Nguyen et al. (2014) experimentally observed overall particle size reduction in unconsolidated sand due to particle breakage in compaction bands. In compaction tests on porous sandstone, Cheung et al. (2012) observed more damage on smaller grains, including microcracks and pervasive crushing from two samples, while larger particles remained intact in both experiments.

The macroscopic compaction band may form due to the accumulation of microcracks in the matrix (Vajdova et al., 2004). Heap et al. (2015) showed that compaction band formation is time-dependent. Compaction bands can develop gradually in sandstone reservoirs that consist of well-graded grains, but then suddenly and severely impact permeability.

Moreover, transient propagating and oscillatory behaviours of compaction bands are observed in brittle porous media, including rocks (Vajdova et al., 2004), cereal packs (Valdes et al., 2012; Guillard et al., 2015), and snow (Barraclough et al., 2017). Blatny et al. (2022) presents different patterns of compaction band propagation and oscillation due to different loading rates and yield strengths, as presented in Figure 2.4(c). These patterns initiated naturally from structural deformations leading to universal pore collapse (Blatny et al., 2022).

2.3.2 Influence of compaction bands on permeability

The formation of compaction bands drastically influences the hydraulic conductivity of granulate systems. Compaction bands are characterised by lower porosity and permeability than the surrounding host rock. Therefore, they are widely recognised as hydraulic barriers (Vajdova et al., 2004; Heap et al., 2015). During compressive deformation, the permeability reduction is more significant inside the compaction localisation than within diffuse compaction bands. Holcomb and Olsson (2003) and Vajdova et al. (2004) measured the permeability of Castlegate sandstone and Bentheim sandstone, respectively, and they observed decreases in permeability by two orders of magnitude. More recent permeability measurements in

Diemelstadt sandstone (Baud et al., 2012) and Aztec Sandstone (Deng et al., 2015) also show that compaction bands can reduce permeability by up to four orders of magnitude. In comparison, the permeability drop in diffuse compaction bands (such as in Berea sandstone) is generally more gradual with increasing strain (Zhu et al., 1997). The significance of permeability reduction in compaction bands is dominated by the suppression mechanism of pore spaces (by grain crushing and pore collapse), which is associated with the decrease in the pore size and connectivity, and the increase in the geometric tortuosity (Zhu et al., 1997; Vajdova et al., 2004). Due to the anisotropic suppression of pore spaces, compaction bands also induce anisotropy in hydraulic properties (Vajdova et al., 2004).

2.4 Hydraulic conductivity

An accurate estimation of permeability in porous media is of great concern in various applications, including geotechnical engineering, hydrogeology, petroleum engineering, and underground hydrogen storage. Granular formations receive attention due to their significant prevalence across multiple engineering applications. Granular porous media, fully or partially saturated, are widely found in natural and artificial formations (Chapuis, 2004; Sun et al., 2011; Zheng et al., 2018; Wang et al., 2019). This study focuses on the permeability estimation in fully saturated granular porous media.

2.4.1 Definition of permeability

Fluid transport in porous media is driven by a pressure drop, as illustrated in Figure 2.5(a). At low flow velocity, there is an empirical linear relationship between the pressure gradient and the flow velocity:

$$-\frac{\partial p}{\partial X} = (\mu/k) \cdot q, \tag{2.12}$$

where $\frac{\partial p}{\partial X}$ = pressure gradient in the flow direction X (Pa/m); μ = viscosity of fluid $(kg/(m \cdot s))$; k = permeability (m^2); and q = flow rate (velocity) in the flow direction (m/s). Eq. (2.12) is also known as Darcy's law, in which k represents the permeability of the porous medium. The empirical nature of this relationship has motivated researchers to establish theoretical foundations for it. Whitaker (1969) derived the permeability tensor under low

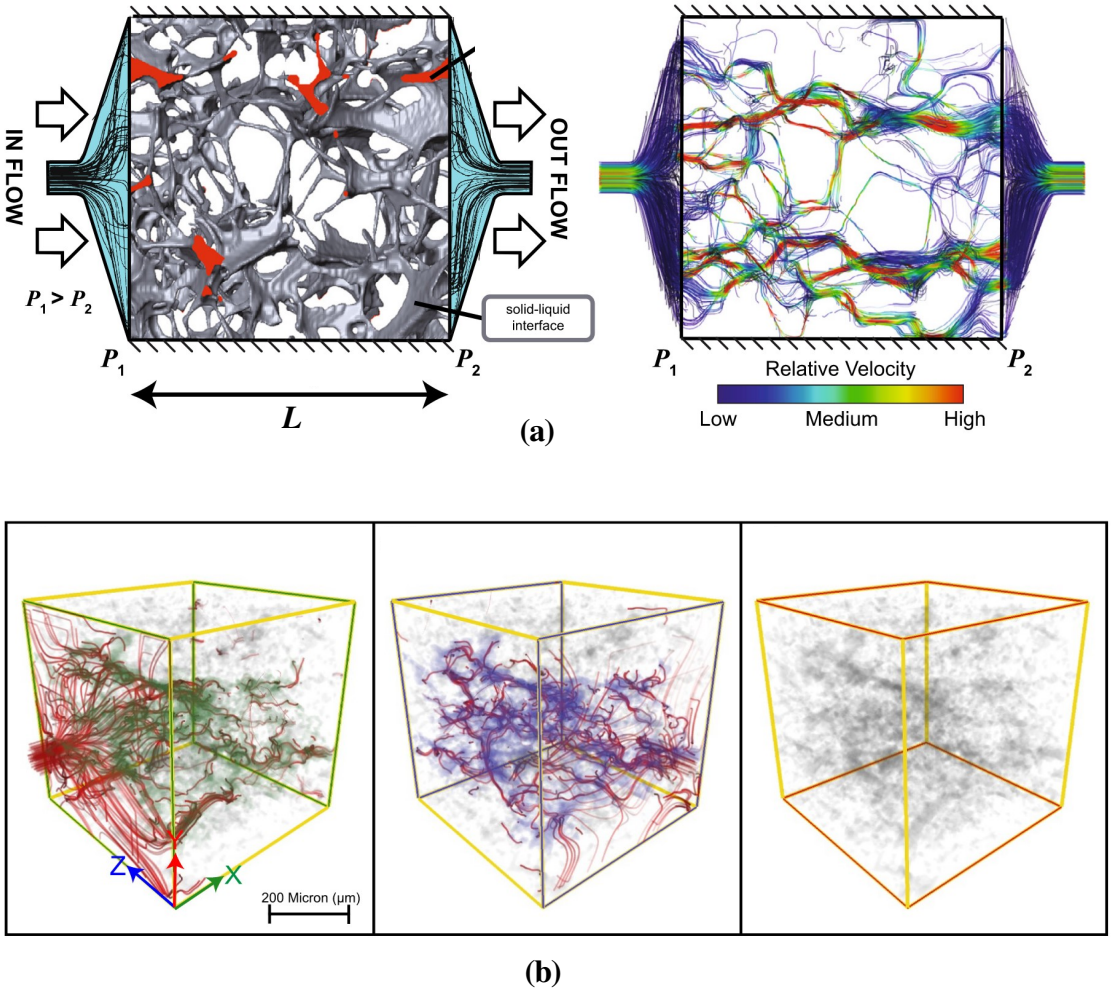

FIGURE 2.5: Illustration of fluid flow through porous media. (a) The pressure difference drives the flow at the in-flow and out-flow. (adopted from Miller et al., 2014) (b) Flow streamlines in the X- Z- and Y-direction (from left to right) through the same porous medium, where disconnected pores are visualised in grey (adopted from Bader et al., 2024).

velocity conditions using the volumetric averaging theory. Hassanizadeh and Gray (1980) mathematically described the macroscopic flow behaviour using a continuum approach.

However, Darcy's law only remains valid under limited conditions. The relationship between the pressure gradient and the flow velocity becomes non-linear at high flow velocities. Forchheimer (1901) modified Darcy's equation by adding a second-order velocity term to represent the microscopic inertial effect:

$$-\frac{\partial p}{\partial X} = (\mu/k) \cdot q + \beta \rho q^2, \tag{2.13}$$

where $\beta =$ the Forchheimer coefficient and $\rho =$ the fluid density.

Moreover, Brinkman (1949) modified Darcy's law by adding the second-order velocity derivatives to include the macroscopic shearing effect at the pore-solid interface:

$$-\frac{\partial p}{\partial X} = \frac{\mu v}{k} - \mu\left(\frac{\partial^2 v}{\partial Y^2} + \frac{\partial^2 v}{\partial Z^2}\right), \tag{2.14}$$

where X, Y and Z are mutually perpendicular directions.

The deviation from Darcy's law becomes negligible when the flow rate is sufficiently slow or the pore channels are sufficiently wide. The Reynolds number ($Re = \frac{\rho dq}{\mu}$, where d =characteristic length) or the Forchheimer number ($F_o = \frac{k_0 \beta \rho q}{\mu}$) provide quantitative criteria for assessing the applicability of Darcy's law. Zeng and Grigg (2006) pointed out that the lack of a definitive characteristic length in the calculation of the Reynolds number has led to a wide range of reported criteria ($0.1 - 1000$). Zeng and Grigg (2006) recommended using a critical Forchheimer number $F_o = \frac{E_c}{1-E_c}$ as the criterion, where E_c represents a limit of the non-Darcy effect. For instance, limiting the acceptable deviation to $E_c = 10\%$ gives a critical F_o of 0.11.

When fluid flows through a homogeneous porous material, a pressure gradient develops within the material due to flow resistance. The experimental methods used to measure permeability, k, generally involve the application of Darcy's law.

2.4.2 Classical permeability equations

The permeability of a granular porous medium depends on the micro-scale properties of both the particles and the pores. Hazen (1892, 1911) developed a formula estimating the permeability based on the particle size of saturated sands:

$$k = C_H D_{10}^2, \tag{2.15}$$

where k =permeability (cm/s); C_H =Hazen empirical coefficient; and D_{10} =particle size for which 10% of the soil is finer (cm). Carrier III (2003) summarised a wide range of C_H values (from 1 to 1000) appearing in textbooks, and pointed out the coefficient's temperature dependence ($C_H = 0.70 + 0.03T$, where T is the temperature in degrees Celsius). Due to the temperature dependence of C_H and other hydraulic behaviours, such as flow resistance,

the Hazen formula requires temperature corrections that significantly complicate its practical application for an accurate permeability estimation.

Subsequently, Kozeny (1927) and Carman (1939) developed the following semi-empirical, semi-theoretical Kozeny-Carman equation for permeability estimation in fully saturated porous media:

$$k = \left(\frac{\gamma}{\mu}\right)\left(\frac{1}{C_{K-C}}\right)\left(\frac{1}{S_0}\right)\left[\frac{e^3}{1+e}\right], \tag{2.16}$$

where γ = unit weight of fluid; μ = viscosity of fluid; C_{K-C} = Kozeny-Carman empirical coefficient; S_0 = specific surface area per unit volume of particles (1/cm); and e = void ratio. At $20°C$, $\gamma/\mu = 59.933$ 1/cm s. Carman (1956) reported that $C_{K-C} = 4.8 \pm 0.3$ for uniform spheres, although a slightly wider range $C_{K-C} < 6.4$ is also within relevant experimental values.

This semi-empirical, semi-theoretical formula Eq. (2.16), covers the effect of particle size indirectly via S_0 and a wide range of particle shape via C_{K-C} - The value of C_{K-C} is found to be around 5 for mono-dispersed spheres (Carman, 1939), around 3.4 for peat beds (Mathavan & Viraraghavan, 1992), and around 12.81 for a mixture of fibrous and granular beds (Li & Gu, 2005). When all grains are spherical, the shape coefficient C_{K-C} can be removed from the Kozeny-Carman equation (Eq. (2.16)) to focus on the particle size effect (Carrier III, 2003):

$$k = 0.083 \times \gamma/\mu \times \frac{e^3}{1+e} \times d_{10}^2. \tag{2.17}$$

2.4.3 Dependence on microscale features

Permeability in granular materials depends on particle characteristics and their spatial arrangement. While the Kozeny-Carman equation (Eq. (2.16)) captures basic relationships between the porosity, specific surface area, and permeability, it cannot fully represent the hydraulic behaviour in real granular systems with the interplay of particle size, shape, and packing heterogeneity. Recent imaging and computational advances reveal how microscale features control macroscopic transport properties through both static pore geometry and its evolution during deformation.

Particle size controls the permeability primarily through pore dimensions (Keller & Holzer, 2018). The effect of particle size on permeability is captured by the Kozeny-Carman equation

via the specific surface area S_0 and the void ratio e. The magnitude of permeability k is highly sensitive to the void ratio, which is controlled by the particle size distribution. In the experiment (*e.g.*, Wei et al., 2021) and numerical study (*e.g.*, Kerimov et al., 2018), the particle size was repeatedly confirmed to be the dominating factor of permeability.

Particle size distribution also controls the permeability in granular materials. In polydisperse systems, smaller particles fill voids between larger grains, increase the tortuosity, and suppress permeability (Kerimov et al., 2018). This effect is typically covered by the coefficient C_{K-C} in the Kozeny-Carman equation.

Particle morphology affects permeability through flow path tortuosity and specific surface area. Angular particles reduce permeability by 300-500% compared to spheres due to enhanced flow separation (Zhao & O'Sullivan, 2022). Wei et al. (2021) demonstrated that the particle surface roughness could be captured by the specific surface area when measured accurately. Particle shape also controls permeability via the void ratio. After confinement, angular particles often maintain higher porosity while spheres achieve denser arrangement (Kerimov et al., 2018).

Local heterogeneity in porosity and pore throat distribution creates preferential flow paths that determine the effective permeability. Natural granular media may exhibit heterogeneity, such as preferentially oriented pore connectivity and disconnected pores causing permeability anisotropy, as indicated by streamlines in Figure 2.5(b). Through computational fluid dynamics, Zhao and O'Sullivan (2022) confirmed that local heterogeneities lead to a few large pores acting as preferential flow paths with substantially higher flow rates.

The permeability in granular materials evolves during deformation via the alteration of particle size, shape, and arrangement (Wang et al., 2016). Possible occurrences of strain localisation may induce heterogeneity with pore collapse, fine migration, and microcracking, reduce the permeability locally by orders of magnitude while the surrounding granular matrix remains unaffected (Heap et al., 2024).

2.5 Summary

Based on related literature reviews, the particle size and shape fundamentally control the mechanical and hydraulic behaviours of granular materials through contact mechanics and pore

structures. Previous studies have extensively investigated the formation of breakage-induced compaction bands and their influences on permeability, while these effects in shape-induced strain localisations are rarely discussed. The reviewed methods for particle reconstruction using spherical harmonics, fabric quantification through DEM and image analysis, and permeability estimation via computational approaches provided the theoretical foundation for this study. The following chapters will systematically present our approaches to systematically investigate how controlled variations in the fractal dimension and surface roughness of particles affect the evolution of particle- and pore-orientation fabrics, and to establish relationships between fabric anisotropy and directional permeability in granular assemblies without particle breakage.

CHAPTER 3

Methodology

In this chapter, we focus on the methodology of numerically realising shape-induced compaction bands and estimating their permeability. We demonstrate the method to virtually generate irregular particles via Fourier transforms of spherical harmonics (SH), to numerically simulate compaction bands with virtual particles using the discrete element method (DEM), to quantify the fabric in the simulated granular assembly, and to estimate the permeability from the granular assembly via computational fluid dynamics (CFD).

3.1 Reconstructing 3D realistic particles

In this study, we implemented 3D Fourier transforms on Spherical Harmonic (SH) functions to reconstruct star-like convex surfaces of natural grains via approximating the cumulative radial distance between surface points and their centroid. In a polar coordinate system, the cumulative radial distance $r_I$of the I_{th} particle can be written as a function of the latitudinal coordinate $\theta \in [0, \pi]$ and the longitudinal coordinate $\phi \in [0, 2\pi]$, as presented by Equation 2.6, which is repeated here for easy reference:

$$r(\theta, \phi) = \sum_{n=0}^{\infty} \sum_{m=-n}^{n} c_n^m Y_n^m(\theta, \phi), \tag{3.1}$$

where c_n^m are the coefficients of SH frequencies $Y_n^m(\theta, \phi)$, which are defined by Equation 3.2:

$$Y_n^m(\theta, \phi) = \sqrt{\frac{(2n+1)(n-m)!}{4\pi(n+m)!}} P_n^m(\cos\theta) e^{im\phi}, \tag{3.2}$$

where n and m are the degree and the order of the associated Legendre function $P_n^m(x)$, which is defined by Rodrigues's formula (Askey, 2005):

$$P_n^m(x) = (1-x^2)^{|m|/2} \cdot \frac{d^{|m|}}{dx^{|m|}} \left[\frac{1}{2^n n!} \cdot \frac{d^n}{dx^n}(x^2-1)^n \right]. \tag{3.3}$$

According to Equation 2.6 or Equation 3.1, the amplitude of a number of different SH frequencies determines the intensities of morphological features on the reconstructed particle surface. The amplitude at each spherical harmonic frequency can be measured by:

$$L_n = \sqrt{\sum_{m=-n}^{n} \|c_n^m\|^2} \quad , \tag{3.4}$$

where $||.||$ is the second-order norm.

Wei et al. (2018) reconstructed real Leighton Buzzard sand particles from their CT images, and found varying contributions of different SH frequencies indicated by different magnitudes of L_n. Specifically, they concluded that L_0 represents the particle volume, L_2 to L_4 represent the general shape of the particle, L_5 to L_8 represent the local roundness of the particle, and L_9 to L_{15} represent the surface texture of the particle. Interestingly, L_1 only represents a shift of the reconstructed particle profile with respect to the original centroid position but does not influence the particle morphology. Although higher degrees could improve the modelling of particle morphology features at the roughness-length scale, they are rarely implemented in numerical models due to the computational efficiency required for relevant mechanical or hydraulic simulations.

Wei et al. (2018) empirically quantified the development rule of the amplitudes L_n as a function of the particle shape:

$$D_n = D_2 \cdot (\frac{n}{2})^{2D_f - 6}, \tag{3.5}$$

where $D_n = L_n/L_0$ ($n = 2, 3, 4, 5, ..., 15$) is the normalised amplitude of the SH frequency at degree n, and D_f represents the fractal dimension of the particle morphology.

Wei et al. (2021) further quantified the relative roughness of SH-reconstructed particles. The relative roughness R_r of each reconstructed particle quantifies the global difference between its irregular surface and its L_0- or c_0-determined sphere. According to the Parseval formula, the mean square distance (M_{SD}) between two SH surfaces can be directly computed from their

SH coefficients $c_{1,n}^m$ and $c_{2,n}^m$ (Gerig et al., 2001): $M_{SD} = \frac{1}{4\pi}\sum_{n=0}^{\infty}\sum_{m=-n}^{n}\|c_{1,n}^m - c_{2,n}^m\|^2$. Consequently, we can define the relative roughness R_r based on $\sqrt{M_{SD}}$:

$$R_r = \sqrt{\frac{\frac{1}{4\pi}\sum_{n=2}^{n_{\max}}\sum_{m=-n}^{n}\|c_n^m\|^2}{c_0^0\cdot\gamma_0^0(\theta,\phi)}} = \sqrt{\sum_{n=2}^{n_{\max}}\left(D_2\cdot\left(\frac{n}{2}\right)^{2D_r-6}\right)^2}. \tag{3.6}$$

In the current study, n_{max} is set to 15, which is sufficient in depicting morphology features related to surface roughness.

We implemented the SH-based method to generate realistic Leighton Buzzard sand particles, controlling size, angularity, and surface roughness by manipulating SH-coefficients c_n^m. Countless possible combinations of c_n^m exist in the Fourier transform (Equation 2.6 or Equation 3.1) to satisfy the relation defined by Equation 3.5. For the subsequent simulation of granular packing, we systematically generated thousands of unique convex particle shapes for each exclusive pair of SH shape parameters R_r and D_f. Smooth spheres were generated with $R_r = 0.00$ and $D_f = 2.00$, and irregular particles representing natural Leighton Buzzard sands were generated using $R_r = 0.138$ and $D_f = 2.11$ (Wei et al., 2021). To model other irregular particle shapes, a range of R_r and D_f values ($R_r = 0.03, 0.06, 0.10$ and $D_f = 2.10, 2.15, 2.20, 2.30$) was implemented.

3.2 Numerical modelling of strain localisation

In this study, we numerically set up granular assemblies with prescribed initial fabric and compressed them in an oedometer test condition. Considering the direction of particles' major axes (θ, ϕ), We assembled two varieties of initial fabric - one with a random azimuth angle $\theta \in [0, 2\pi]$ and a polar angle $\phi \in [0, \pi]$, one with $\theta = 0$ and $\phi = 0$. We implemented DEM via Ansys Rocky 2024 R1 to deform each initially isotropic or aligned granular assembly: we inserted particles in prescribed orientations without overlaps, isotropically compacted the grains into a dense state, and applied one-dimensional loading with rigid lateral constraints.

In this section, we first illustrate the workflow for validating the DEM implementation using micro-CT images and constitutive relations from experiments. Then, we present the setup in the numerical oedometer tests, including details about particle insertion, isotropic compaction, and one-dimensional oedometer compression.

3.2.1 Validating the discrete element method

The micro-CT results used in this study were reported by Zhao et al. (2020), who performed uniaxial compression on mini samples of Leighton Buzzard sand (LBS) with in-situ CT scanning. Each sample had an equal diameter and height of 6 mm and contained approximately 308 grains with a size range of 0.6 to 1.18 mm. The samples were compressed under quasi-static conditions while particles rearranged and progressively fractured under compressive loading. The compression was paused at several vertical stress levels for CT scanning, including 1 MPa and 10 MPa corresponding to vertical strains of 0.75% and 4%, respectively.

A series of image-processing techniques was adopted to separate individual particles. First, the images at 0.75% vertical strain were filtered to remove noise and small artefacts. Then, we employed the watershed algorithm (Beucher & Meyer, 2018) to identify preliminary particle boundaries based on local intensity gradients. A distance map was computed, and the H-maxima transformation was applied to refine the segmentation. Lastly, each connected component was labelled with a unique integer to identify a segmented particle. In this process, only the H-maxima value is adjusted, and it controls the aggressiveness of the segmentation. The optimal H-maxima value was determined through iterative visual inspection to balance over-segmentation and under-segmentation. The remaining over-segmented fragments or under-segmented agglomerates were merged or separated. The number of particles eventually matches the original count from the experiment.

Then, the surface morphology of individual particles is reconstructed and repaired for DEM simulation. The initial three-dimensional surface meshes were generated from the segmented CT data using MATLAB. The resulting stereolithography (STL) files were processed through Formware (Formware, 2025), an online mesh repair tool, to eliminate topological defects such as non-manifold edges, inverted normals, and self-intersections. Some fixed geometries still contain reconstruction artefacts and unrealistic surface features; these are manually removed in Blender to ensure the mesh reasonably represents the morphology of the original particles.

After obtaining the virtual models of individual grains with reconstructed morphology, we load the grain models into a DEM simulation replicating the experimental configuration at 0.75% vertical strain from (Zhao et al., 2020). Note that the initial confining pressure was zero at this state with no particle overlapping, although the corresponding stress was 1 MPa in the

TABLE 3.1: Sample properties (Wu et al., 2022)

Parameter	Value
Particles (Quartz)	
Density: kg/m^3	2650
Young's modulus: GPa	66.7
Poisson's ratio	0.15
Platens (Ceramic)	
Density: kg/m^3	7850
Young's modulus: GPa	350
Poisson's ratio	0.22
Interactions	
Friction coefficient	0.5
Damping coefficient	0.2

physical experiment. The DEM simulation employed a Hertz-Mindlin linear contact model and zero rolling resistance, as that is achieved by the inherent interlocking between irregular particles. The material properties were set mostly following (Wu et al., 2022), as presented in Table 3.1. To ensure a quasi-static condition, the top platen was accelerated from rest to 0.01 m/s over the first 0.01 second and maintained this constant loading rate for the remainder of the simulation. The friction coefficient between all components in the DEM simulation is kept identical for simplicity. We tested several friction coefficients ($\mu = 0.2, 0.4, 0.5, 0.6$) and compared their resulting stress-strain behaviour against the original experiment, as shown in Figure 3.1, among which $\mu = 0.5$ yielded the best alignment towards the left of the plots where little particle breakage happens in the experiment.

3.2.2 DEM model set-up

We systematically generated virtual particles with different morphologies and simulated their mechanical response using DEM. Figure 3.2 illustrates the workflow from the particle generation in various shapes to the DEM model set-up.

To systematically investigate the influence of particle morphology on fabric and permeability anisotropy due to strain localisation, we numerically simulated compaction bands using DEM in ANSYS Rocky 2024 R1. The implementation builds upon our validated model while extending the analysis to controlled variations in particle shape parameters. The material properties, interaction models, and parameters were selected according to the validation

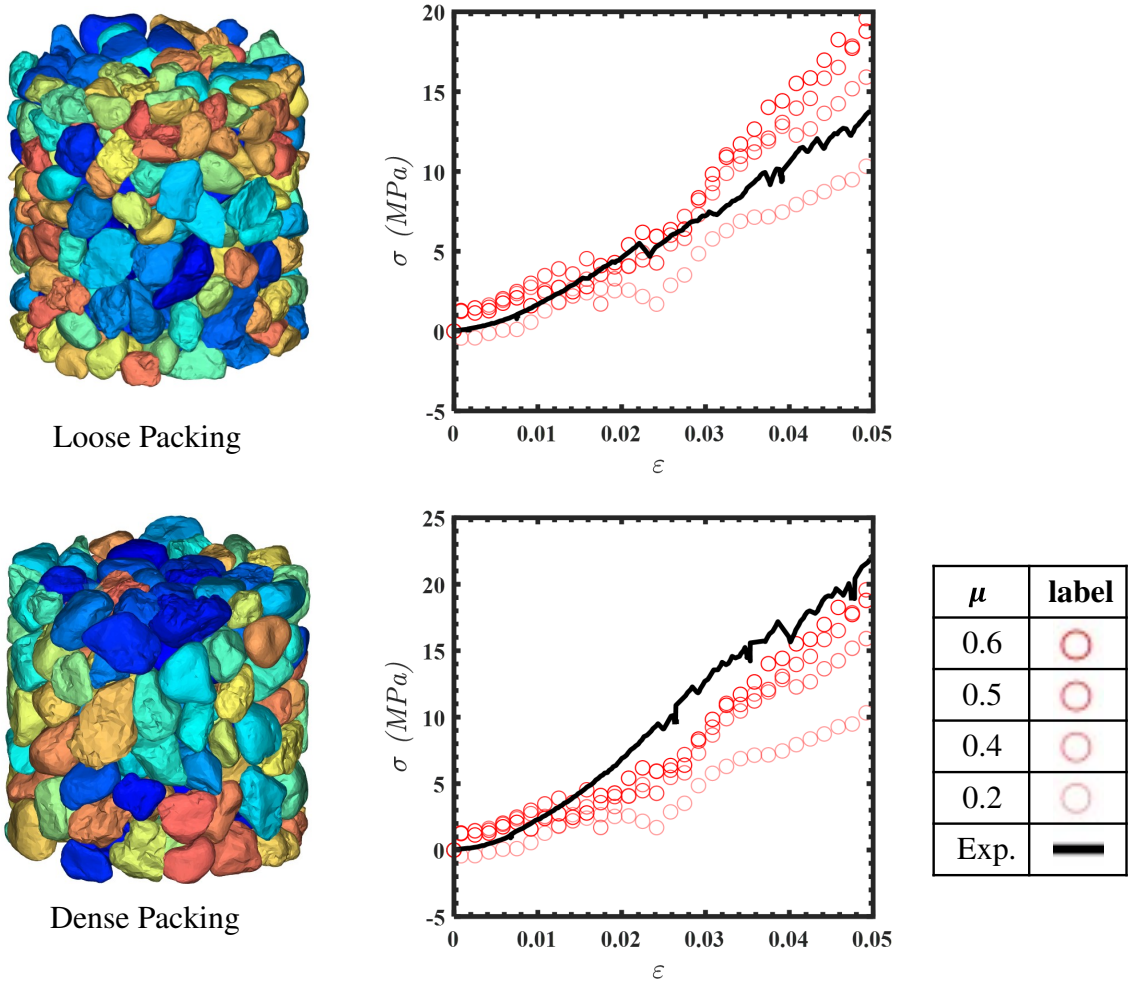

FIGURE 3.1: DEM parameter calibration: vertical stress - strain. The experiment data was adopted from (Zhao et al., 2020).

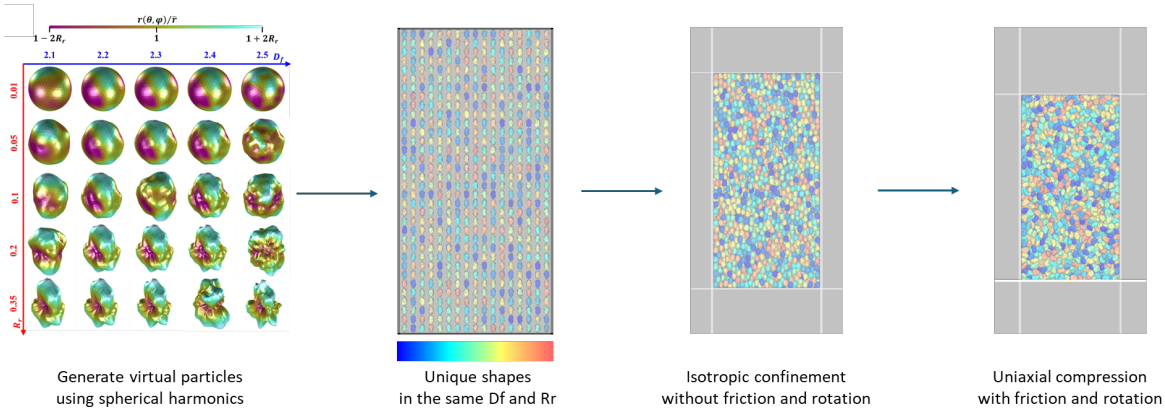

FIGURE 3.2: Particle generation and DEM set-up. The particle shape matrix was adopted from (Suo et al., 2024).

outcome (*i.e.*, $\mu = 0.5$; and others in Table 3.1). And the particle shape was controlled via SH-shape parameters D_f and R_r in the morphology reconstruction process. We leverage Ansys Rocky's capability to handle concave polyhedral particle surfaces with detailed morphological

features (captured by 1280 faces per particle in the current study) and enable a realistic representation of irregular grain morphologies.

For the particle generation, we employed spherical harmonics (SH) to reconstruct irregular particles with quantitative control of morphological characteristics. All particles maintained a consistent volume-equivalent diameter of 2 mm, while varying morphology is obtained through different combinations of the fractal dimension (D_f) and relative roughness (R_r). This approach allows us to isolate the effect of specific shape parameters to investigate the shape-dependent mechanical behaviours of granular assemblies during compaction.

As illustrated in Figure 3.2, each particle shape is generated using spherical harmonics and converted into a closed facet geometry, then imported directly into Ansys Rocky as a custom polyhedron. Unlike conventional DEM codes that approximate non-spherical particles using overlapping multi-sphere clumps (Zhou et al., 2016), Ansys Rocky resolves contact interactions directly on the polyhedral surface, handling vertex-to-vertex, vertex-to-edge, vertex-to-face, edge-to-edge, edge-to-face, and face-to-face contact scenarios (Ansys, 2024). Resolving contacts directly on the polyhedral surface preserves accurate particle geometry, including sharp corners and edges.

The DEM simulations were set up to represent a cubic container with dimensions of 17×17×34 particle diameters (length $\times$ width $\times$ height) at the defined zero strain. There were 9826 particles in the simulation to ensure statistical representativeness while maintaining computational efficiency. To simulate the interlocking placement of particles in dense granular assemblies, we placed the particles on a grid (51mm $\times$ 51mm $\times$ 102mm) 1.5 times larger than the contained at zero strain (34mm $\times$ 34mm $\times$ 68mm) and isotropically compressed the six boundaries to a strain of 2.98%, which was the strain of the dense state from experiments of Zhao et al. (2020). The multiplier 1.5 was selected to ensure zero particle overlapping at the initial placement.

The boundaries were moving towards the centre of the container at decelerating speeds. The four walls in the lateral directions and the two platens at the top and bottom were assigned an initial velocity of 0.2 m/s and 0.4 m/s, respectively. And all six boundaries were slowing down linearly over time until being stationary at 0.09 seconds, followed by an equivalent rest period of 0.09 seconds.

We tested two types of initial particle placement: i) random particle orientations, and ii) identical orientation with principal axes of all particles aligned vertically (the direction of height). In all simulations, we relaxed all degrees of freedom of the particles, except for the isotropic compression in particle placement type ii) to maintain the alignment of particle orientation until the uniaxial compression later.

Following the previous calibration, we applied the Hertz-Mindlin contact model with a hysteric damping coefficient of 0.2 and a friction coefficient of 0.5 throughout the simulation, except for a temporary disablement of the friction coefficient through the 0.09-second duration of the isotropic compression. This temporary frictionless condition facilitated more particle rearrangement from the initial grid placements into natural dense packing configurations, as illustrated in Figure 3.2.

Following isotropic confinement, uniaxial compression was applied to induce compaction band formation. The top ceramic platen was driven downwards at a constant velocity of 0.01 m/s for 0.5 seconds. The total vertical strain is sufficiently large to capture the formation and propagation of compaction bands, and the loading velocity is sufficiently small to maintain quasi-static conditions while ensuring computation efficiency. A longer loading duration may yield greater deformation, enabling further capture of compaction band propagation; however, this may result in unrealistic grain movement due to the absence of fractures in our DEM simulations.

To enable the analysis of micro-structural evolution during compaction, particle coordinates and orientations were recorded every 0.01 second throughout the simulations. These particulate data could provide direct computation of strain rate and fabric tensor evolution, offering insights into the micro-mechanical processes of compaction band formation.

The resulting datasets enabled quantitative correlation between particle-scale properties and macroscopic behaviour, in particular, the relationship between particle morphology, fabric anisotropy, and permeability characteristics within and around compaction bands.

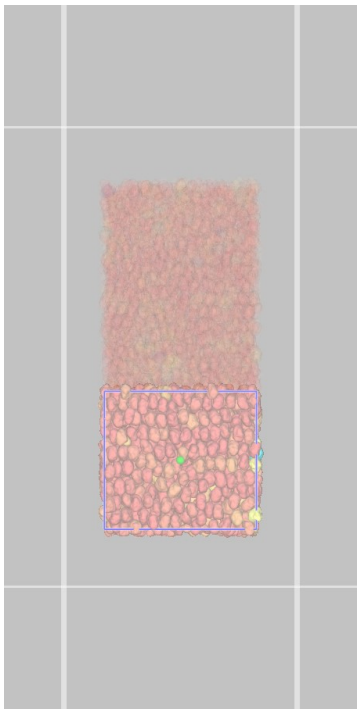

FIGURE 3.3: An example of the moving window for quantifying local strain rate, porosity, and fabric in a granular assembly. The blue box indicates the measurement window that traverses vertically within the semi-transparent region. The measurement zone maintains a 3-particle-diameter buffer from all boundaries to avoid edge effects.

3.3 Tracking strain localisation in DEM simulations

Compaction bands are strain-localisation zones with higher strain rates, more collapsed pores, and more disoriented particles. To track the spatiotemporal evolution of compaction bands, we quantified strain rate, porosity, and particle-orientation fabric within moving windows. As depicted in Figure 3.3, the moving windows were taken from the measurement zone which keeps a 3-particle-diameter buffer from all boundaries. The windows were 10 particles tall and were sampled with a vertical increment of 1% height of the measurement zone. The strain rate, porosity, and fabric at the centroid height of each window position were computed based on the data of the particles within the window.

3.3.1 Strain rate

Each moving-window position corresponds to a region of interest containing multiple particles, the velocity and coordinate of which can be collected to calculate the Cauchy's strain tensor

at the position, as:

$$\dot{\varepsilon_{\mathbf{ij}}} = \frac{1}{2}(\mathbf{u_{i,j}} + \mathbf{u_{j,i}}), \tag{3.7}$$

where $\dot{\varepsilon_{\mathbf{ij}}}$ is the Cauchy's strain tensor, and $\mathbf{u_{i,j}}$ is the gradient of the i-component of velocity in the j-direction. This equation could also be written in different annotations:

$$\begin{bmatrix} \dot{\varepsilon_{xx}} & \dot{\varepsilon_{xy}} & \dot{\varepsilon_{xz}} \\ \dot{\varepsilon_{yx}} & \dot{\varepsilon_{yy}} & \dot{\varepsilon_{yz}} \\ \dot{\varepsilon_{zx}} & \dot{\varepsilon_{zy}} & \dot{\varepsilon_{zz}} \end{bmatrix} = \begin{bmatrix} \frac{\partial u_x}{\partial x} & \frac{1}{2}\left(\frac{\partial u_x}{\partial y} + \frac{\partial u_y}{\partial x}\right) & \frac{1}{2}\left(\frac{\partial u_x}{\partial z} + \frac{\partial u_z}{\partial x}\right) \\ \frac{1}{2}\left(\frac{\partial u_y}{\partial x} + \frac{\partial u_x}{\partial y}\right) & \frac{\partial u_y}{\partial y} & \frac{1}{2}\left(\frac{\partial u_y}{\partial z} + \frac{\partial u_z}{\partial y}\right) \\ \frac{1}{2}\left(\frac{\partial u_z}{\partial x} + \frac{\partial u_x}{\partial z}\right) & \frac{1}{2}\left(\frac{\partial u_z}{\partial y} + \frac{\partial u_y}{\partial z}\right) & \frac{\partial u_z}{\partial z} \end{bmatrix}. \tag{3.8}$$

Based on Cauchy's strain tensor, an equivalent strain rate $\dot{\bar{\varepsilon}}$ can be obtained at the moving-window position via double contraction:

$$\dot{\bar{\varepsilon}} = \sqrt{(\dot{\varepsilon_{\mathbf{ij}}} : \dot{\varepsilon_{\mathbf{ij}}})}. \tag{3.9}$$

3.3.2 Porosity

Porosity is defined as the volume ratio of the pore space within granular media. In a moving window, the porosity is estimated from the volume of the spatial window and the included particles. In the DEM simulations, all particles are identical in size, with a volume equal to that of a sphere with a 2-mm diameter (*i.e.*, $r = 1$ mm). Based on the volume $V_{\mathrm{moving-window}}$ and the number of included particles n_{included}, the porosity ϕ at the moving-window position can be estimated as:

$$\phi = \frac{V_{\mathrm{moving-window}} - n_{\mathrm{included}} \cdot \frac{4}{3}\pi r^3}{V_{\mathrm{moving-window}}}. \tag{3.10}$$

3.3.3 Particle orientation fabric

The orientation of individual particles in three-dimensional space is characterised by their principal axes determined through Principal Component Analysis (PCA). For each particle, the inertia tensor is constructed from the coordinates of its constituent voxels or vertices (Fonseca et al., 2013):

$$\mathbf{I}_{ij} = \sum_{k=1}^{N_p} m_k(r_k^2\delta_{ij} - r_{ki}r_{kj}), \tag{3.11}$$

where N_p is the number of vertices, m_k is the mass,

For elongated particles, their orientation is defined as the unit vector n aligning with the major principal axis. The orientation can be expressed in spherical coordinates as (β, γ), where β represents the polar inclination angle from the vertical z-axis ($0 \leq \beta \leq \pi$) and γ denotes the azimuthal angle ($0 \leq \gamma \leq 2\pi$).

For an assembly of N particles with uniform size distribution, the fabric tensor quantifies the average directional bias of particle orientations. Repeating Equation 2.8, the second-order fabric tensor is computed as:

$$\Phi_{ij} = \frac{1}{N} \sum_{k=1}^{N} n_i^k n_j^k. \tag{3.12}$$

And repeating Equation 2.11, the deviator fabric is calculated as:

$$\Phi_d = \frac{1}{\sqrt{2}} \sqrt{(\Phi_1 - \Phi_2)^2 + (\Phi_2 - \Phi_3)^2 + (\Phi_3 - \Phi_1)^2}, \tag{3.13}$$

which provides a scalar measure of directional preference, ranging from 0 for isotropic arrangements to 1 for perfectly aligned particles. The primary fabric direction aligns with the eigenvector corresponding to Φ_1.

3.4 Quantifying pore-space anisotropy in DEM simulations

The quantification of fabric anisotropy in granular materials requires systematic measurements that focus on different geometric components. Fabric analysis is performed within designated regions of interest to capture the directional characteristics of both particles and pores. For particle orientation fabric, quantification occurs within moving windows to track the spatiotemporal evolution of compaction band formation, as illustrated previously. In this section, we first outline the procedure for analysing pore-orientation fabric within cubic representative elementary volumes (REVs). Then, we describe our numerical approach for estimating permeability.

3.4.1 Pore orientation fabric

Upon previous determination of pore orientation fabric, we selected REVs at three intermediate heights from DEM simulations at varying vertical strains (export time). Due to the high computational expenses of LBM, we could not simulate all REVs from all time exports. Thus, we selected several REVs at different time values, based on similarity in porosity or fabric, for further permeability computation. After analysing the virtual granular assemblies using methods in Section 3.3, we obtained the estimated porosity and the particle orientation fabric from the DEM simulations. Mentioning later in the chapter of results and discussions, Figure 4.4 presents the selection of REVs based on comparable D_f and R_r from different heights and loading strain (time).

Those selected REVs were converted into binary voxel representations for the computation of pore orientation fabric via pyfabric and for the permeability simulation using Palabos. We set the image resolution as 100 voxels per particle diameter to ensure sufficient voxels across small pore constrictions. The binary images distinguish pore, solid-pore interface, and solid with integers 0, 1, 2 assigned at voxels (*a.k.a*, lattices), respectively. These binary arrays are formatted into DAT files to be read by Palabos following the converter from the Palabos official package.

Pore orientation fabric characterises the directional distribution of void spaces within granular assemblies, suggesting likely preferential flow pathways and transport anisotropy. Unlike the particle fabric which examines solid phase arrangement, pore fabric quantifies the geometric anisotropy of interconnected void networks that control fluid flow behaviour.

We adopted a pyfabric (Wald et al., 2005; Varga & Zysset, 2009; Varga et al., 2013) workflow to quantify the pore orientation fabric using spatial autocorrelation analysis. This method characterises the directional anisotropy of void spaces by analysing their spatial correlation patterns in three dimensions based on binary images of granular porous media.

In the virtual granular assemblies from DEM simulations, the full height (100%) designated by the distance between the top and bottom platens shortens as the uniaxial compression proceeds. We selected three REVs centred at the three intermediate heights ($30\%, 50\%$, and 70%) corresponding to the shortening full height, and exported their particles every 0.01

second throughout the simulations. As presented by Figure 3.4, the particles bounded by a REV were exported into facet geometries in STL, and we regenerated the REV in a binary image series containing distinct pore and particle voxels.

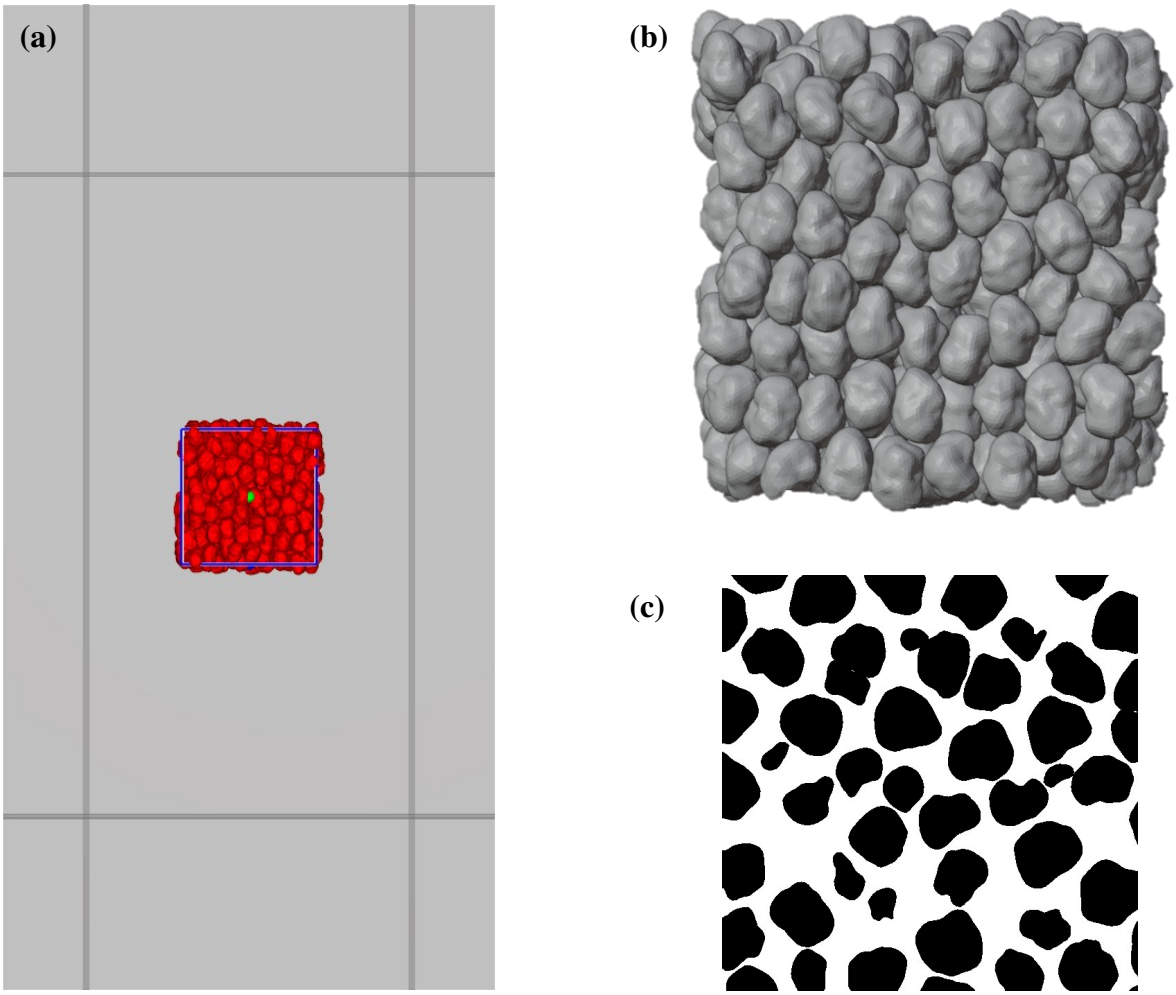

FIGURE 3.4: Selecting REVs from DEM and converting them into binary images. (a) Particles bounded by cubic regions in size 7×7×7 diameter^3 centreing at intermediate heights were selected from DEM simulations. (b) The selected particles were exported into STL. (c) The STL geometry was converted to a binary image series, which was cropped to a 6×6×6 diameter-cubed size.

The pyfabric workflow begins with the computation of the 3D Auto Correlation Function (ACF) from binary segmented pore images. The ACF is calculated in the Fourier domain as:

$$\text{ACF} = \left| \mathcal{F}^{-1} \left[\mathcal{F}(I) \cdot \overline{\mathcal{F}(I)} \right] \right|, \tag{3.14}$$

where I represents the binary image, $\mathcal{F}$ and $\mathcal{F}^{-1}$ denote the discrete Fourier transform of the image and its inverse, and the overbar indicates complex conjugation. The resulting ACF

map quantifies the spatial correlation of pore structures at different separation distances and orientations.

The central region of the ACF was extracted and interpolated with a zoom factor of 2 to enhance resolution. After normalisation to the range [0,1], an isosurface was extracted at a threshold value of 0.4. This threshold was selected to capture the primary correlation structure while avoiding noise from weak correlations. We implemented the marching cubes algorithm to generate a point cloud representing this isosurface.

An ellipsoid was fitted to the point cloud using least-squares optimisation, yielding principal radii (r_1, r_2, r_3) and corresponding eigenvectors that define the pore fabric orientation. Then, the pore fabric tensor was constructed as:

$$\Phi_{ij}^{pore} = \sum_{k=1}^{3} \lambda_k v_i^k v_j^k, \tag{3.15}$$

where $\lambda_k = r_k^{-2} / \sum r_i^{-2}$ are normalised eigenvalues and v^k are the ellipsoid's principal directions. Analogous to the scalar treatment of the particle orientation fabric, we also applied Equation 3.13 to the pore fabric tensor to determine its deviator fabric value Φ_d, ranging from 0 for isotropic arrangements to 1 for perfectly aligned void channels.

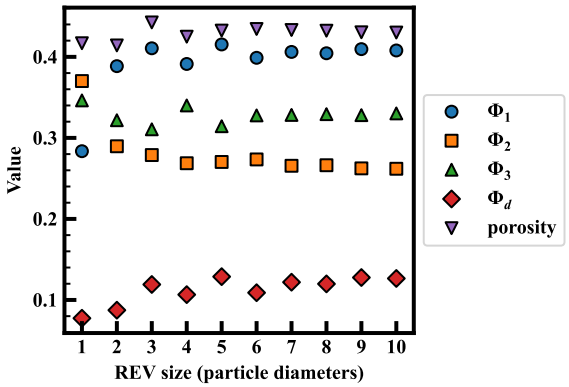

FIGURE 3.5: Convergence of porosity and pore-fabric tensor components Φ_1, Φ_2, and Φ_3 with REV size. Φ_d denotes deviatoric fabric. Values stabilise beyond 5-6 particle diameters.

This study covers dozens of cases covering a range of grain morphology, compaction stages, and flow directions. To balance statistical representativeness with computational efficiency, we performed a sensitivity analysis on REV sizes. Figure 3.5 shows stable porosity and pore-orientation fabric in REVs taken from the centre of a typical virtual assembly of irregular particles. The figure indicates that the pore geometry is statistically consistent in larger REVs

spanning more than five particles, a finding consistent across a wide range of tested morphologies and compaction stages. The specific size of 6×6×6 diameters is used throughout this study.

3.4.2 Computing permeability via computational fluid dynamics

Computational Fluid Dynamics (CFD) can numerically simulate fluid motion through complex flow channels by solving the incompressible Navier-Stokes equations. Although mesh-based solvers exist for the equations, we implemented a mesh-free lattice-based approach for the numerical solution due to intricate difficulties in the mesh generation. Here, we give an introduction to the incompressible Navier-Stokes equations, followed by a brief demonstration of the challenges involved in the mesh generation for the complex pore geometry. Then, we present our lattice-based approach to numerically simulate laminar flow in multiple directions.

3.4.2.1 Governing equations

Fluid flow through porous media at the pore scale is governed by the incompressible Navier-Stokes equations (Batchelor, 2000). For steady-state laminar flow of a Newtonian fluid, the momentum equation is:

$$\frac{\partial \mathbf{u}}{\partial t} + (\mathbf{u} \cdot \nabla)\mathbf{u} = \frac{\mu}{\rho}\nabla^2 \mathbf{u}, \tag{3.16}$$

where u represents the velocity vector, p is pressure, ρ denotes fluid density, μ is dynamic viscosity, and F accounts for body forces. The continuity equation for incompressible flow requires:

$$\nabla \cdot \mathbf{u} = 0. \tag{3.17}$$

At solid-fluid interfaces, the no-slip boundary condition enforces $u = 0$ at particle surfaces. For low Reynolds number flows typical in granular porous media ($Re << 1$), the inertial term $\rho(\mathbf{u} \cdot \nabla)\mathbf{u}$ in the steady state becomes negligible, reducing the momentum equation to the Stokes equation:

$$\nabla p = \mu \nabla^2 u. \tag{3.18}$$

Exact solutions to this equation could only be obtained for simple geometries, such as in the steady-state flow between parallel plates. In more realistic geometries representing rocks, the Navier-Stokes equations must be approximated linearly (Zimmerman & Bodvarsson,

1996). The complex boundary conditions in irregular and interconnected pore structures imposed by interlocking particle arrangement necessitate numerical geometry discretisation into sub-volumes to perform linear solution in.

3.4.2.2 Numerical solver selection

Mesh-based Navier-Stokes solvers face significant challenges in granular porous media applications. The mesh generation for intricate pore geometries requires advanced techniques and extensive computational resources. One approach directly meshes the pore space between particles in their STL facet forms, but facet errors often occur at closely adjacent particle boundaries. In light of this issue, an alternative reconstructs the solid-pore interface using the marching cube algorithm, followed by smoothing to reduce the number of facet triangles; however, the reconstructed surface suffers from compromised water-tightness, especially for fine fluid mesh sizes.

The Lattice Boltzmann Method (LBM) emerges as the optimal mesh-free solver for simulating the hydraulic behaviour of granular porous media. LBM operates on particle collisions within a lattice structure representing voxel geometries, eliminating the need for mesh generation. And it is intrinsically suitable for solving in very complex geometries. LBM operates on particle collisions within a lattice structure representing voxel geometries. In LBM, these fictitious particles represent the statistical distribution of fluid molecules. They undergo collision and streaming steps that collectively reproduce the macroscopic Navier-Stokes equations for fluid flow. These operations are inherently parallelisable to enable the feasibility of computation up to approximately 1000^3 voxels on a modern computer cluster. The number of iterations until convergence is relevant to the relaxation rate, which controls how quickly particle distributions return to equilibrium. The choice of relaxation models and parameters also affects the accuracy of Navier-Stokes solutions.

Palabos is an open-source CFD framework implementing LBM for parallel simulations of complex fluid flows. The library provides a high-level C++ interface for defining geometries, boundary conditions, and multi-physics models while automatically handling parallelisation through the Message Passing Interface (MPI). We employed Palabos to handle single-phase flow for our study.

3.4.2.3 Model setup and validation

The simulations employ the three-dimensional twenty-seven (D3Q27) lattice scheme, which discretises velocity space into 27 directions connecting each lattice node to its neighbours within a cubic neighbourhood. This scheme provides superior isotropy and stability compared to three-dimensional nineteen (D3Q19) alternatives while maintaining computational efficiency Suga et al. (2015). The collision operator uses the single-relaxation-time Bhatnagar-Gross-Krook (BGK) approximation (Timm et al., 2016):

$$f_i(x + c_i\Delta t, t + \Delta t) = f_i(x, t) - \frac{\Delta t}{\tau}(f_i(x, t) - f_i^{eq}(x, t)), \tag{3.19}$$

where f_i represents the particle distribution function along lattice direction i, c_i denotes the discrete velocity vector, τ is the relaxation time related to kinematic viscosity of the fluid through $v = c_s^2(\tau - 0.5)\frac{\Delta x^2}{\Delta t}$ (where c_s is the speed of sound in LBM; Δx and Δt are the physical increment of length and time), and f_i^{eq} is the equilibrium distribution function. We took typical values of $\tau = 1$ and $c_s = \sqrt{1/3} \approx 0.577$ in the standard LBM.

We implemented no-slip boundary conditions at the particle-pore interface using the halfway bounce-back scheme, in which fluid particles colliding with solid boundaries reverse their momentum. This approach accurately positions the no-slip boundary at the midpoint between the fluid and solid nodes, thereby achieving second-order accuracy on curved surfaces. We measured permeability along two lateral directions and one vertical direction of each selected REV. We defined the velocity U^* in lattice units at the inlet and set zero pressure at the outlet, and initialised the models with a uniform flow velocity U^* in the designated flow direction. Following (Kerimov et al., 2018), we assigned no-slip conditions at the four lateral boundaries parallel to the flow direction to calculate the permeability in this direction.

In Palabos, the pressure difference from the inlet to outlet is represented by the density variation $\Delta p^* = c_s^2\Delta\rho^*$, where Δp^* is the pressure difference and $\Delta\rho^*$ is the density variation in lattice units. Palabos iteratively solves to find the spatial distribution of lattice density for the given boundary conditions.

Through iterative calculations, Palabos monitors the convergence of the average kinetic energy density of the fluid field. The kinetic energy density is defined as $E = (1/2)\rho|u|^2$, where ρ represents the local fluid density and $|u|$ denotes the velocity magnitude at each lattice

node. A convergence criterion given by a relative residual $\Delta E < 10^{-4}$ is implemented to indicate when the steady state has been reached in the LBM calculations, where $\Delta E = E_{\mathrm{stand-deviation}}/E_{\mathrm{average}}$. This threshold value ($10^{-4}$) represents an optimal balance between computational efficiency and solution accuracy, ensuring that the flow field has sufficiently stabilised while avoiding unnecessary computational expense.

After reaching the steady state, the lattice density $\Delta\rho^*$ is converted into lattice pressure Δp^* at all fluid lattices. The spatial pressure distribution is further processed into one-dimensional pressure variation along the flow direction by averaging over cross-sections. As depicted in the following Model Validation section, the one-dimensional pressure variation is generally linear within the granular media geometry. A pressure gradient ∇p^* is obtained from the pressure variation.

Then, the permeability k^* is calculated following Darcy's Law (Equation 2.12):

$$-\nabla p^* = (\mu^*/k^*) \cdot U^*, \tag{3.20}$$

where $\mu^* = (1.0 - \Delta\rho^*)(c_s^2(\tau - 0.5))$ is the kinematic viscosity in the lattice unit. The permeability k in the physical unit is obtained as $k = k^*\Delta x^2$.

Granular materials may exhibit differing permeability in different directions. For an REV in 3D, its permeability can be measured from X-, Y-, and Z- directions as k_x, k_y, and k_z, respectively. The degree of anisotropy in the permeability can be represented by k_d, as:

$$k_d = \frac{1}{\sqrt{2}}\sqrt{(k_x - k_y)^2 + (k_y - k_z)^2 + (k_z - k_x)^2}. \tag{3.21}$$

Our numerical setup was validated using a synthesised granular assembly consisting of uniform spheres, enabling a direct comparison with the classical Kozeny-Carman equation.

Figure 3.6 represents the geometry of the sphere particle assembly with the particle diameter of 0.002 m and the porosity of 0.464. The nonuniform packing is generated according to the procedure in the DEM setup section. Due to the round shape of the particles, the granular assembly is considered isotropic. The LBM implementation is validated by simulating laminar flow through this assembly in the Y-direction.

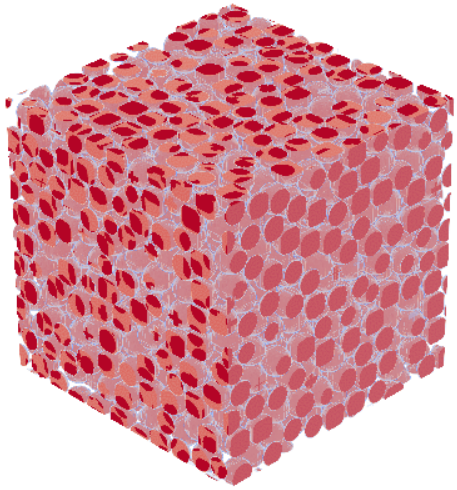

FIGURE 3.6: A virtual granular assembly consists of spheres in their lattice geometry.

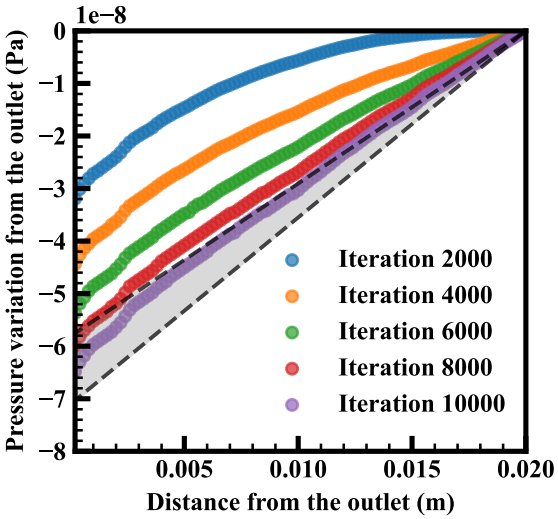

FIGURE 3.7: Iterative change of pressure variation along the flow direction during the solution of LBM. The grey shade between two dashed lines presents the range of permeability estimation from the Kozeny-Carman equation, where the coefficient C_{K-C} is taken as 4.5 and 5.5 at the upper and lower boundaries, respectively.

Boundary conditions are set up, and pressure variations are computed according to the procedure outlined in the previous section. Figure 3.7 shows the pressure variation along the X-direction in the model after different numbers of iterations, compared with the pressure variation estimated from the Kozeny-Carman equation. As the iteration number increases, the pressure data points increasingly approach the Kozeny-Carman estimation. The computed pressure variation has fallen within the range of the Kozeny-Carman predictions since iteration 10000.

3.5 Summary

This chapter presents the computational methodologies for investigating shape-induced strain localisation and the resulting heterogeneous permeability anisotropy in granular materials. The methodology includes three key steps: i) generating irregular particle morphology using Spherical Harmonics (SH), ii) modelling compactive deformation of virtual granular media using the discrete element method (DEM), and iii) estimating local permeability anisotropy using the lattice Boltzmann method (LBM).

We reconstructed realistic irregular particle morphologies using Fourier transform of 15 degrees of spherical harmonics. The morphology was controlled with fractal dimension D_f and relative roughness R_r. To systematically investigate the shape effect on granular behaviours, each DEM simulation contained thousands of unique particles with the same volume, D_f, and R_r. The DEM simulations were validated against mini-triaxial tests of granular material initially undergo deformation with limited breakage to reproduce stress-strain relationships.

Strain localisation zones (*a.k.a.*, compaction bands) in the DEM simulations were tracked through moving windows that captured the spatiotemporal evolution of strain rate, porosity, and particle orientation fabric. Due to limitation of computational resources, dozens of cubic representative elementary volumes (REVs) were extracted at three heights and specific vertical strains where the particle orientation fabric or the porosity were comparable. Within each REV, pore orientation fabric was quantified using autocorrelation analysis, and the permeability was computed via LBM simulations in three orthogonal directions, with validation against the Kozeny-Carman equation for spherical particle assemblies.

This integrated methodology enables quantitative evaluation on the effect of particle morphology on the evolution of fabric and permeability anisotropy in dense granular media under compression, providing insights into the microscopic mechanism of shape-induced strain localisation and permeability evolution.

CHAPTER 4

Results and discussions

In this chapter, we present the results and discussion of strain localisation in DEM simulations, along with the evolution of pore structures and permeability in selected REVs. The first section aims to present evidence of compaction band formation and to discuss the effects of particle shape parameters, namely the roughness R_r and the fractal dimension D_f, on the formation and propagation of compaction bands, as visualised in evolution diagrams of strain rate, porosity, and particle orientation fabric. In the second section, we present CFD results for REVs of mono-dispersed packings with different particle shapes; and we discuss the effect of compaction on the evolution of permeability anisotropy and pore-orientation fabric, and evaluate their correlation. Through the analysis of fabric and permeability, we elaborate the role of particle morphology in causing strain localisation and enhancing permeability anisotropy in dense granular materials under compression.

4.1 Strain localisation in DEM simulations

The combination of geometry, loading conditions, and material properties makes localised deformation energetically favourable over distributed compression in granular materials. This preference for localisation has been demonstrated experimentally by Valdes et al. (2012) in oedometer compaction tests, where the packing of granular puffed rice dissipates energy through localised cracking rather than uniform deformation. When particle breakage is suppressed, as in our DEM simulations with irregular particles, the stick-slip behaviour at interlocked particle contacts provides an alternative energy-dissipation mechanism. Frictional sliding releases energy in discrete stick-slip events analogous to particle breakage, producing strain rate evolution and localisation patterns similar to those observed in experiments

involving particle breakage. The dependence of the stick-slip behaviour on the particle morphology in granular materials is demonstrated in this section.

4.1.1 Contrasting deformation patterns with smooth and rough particles

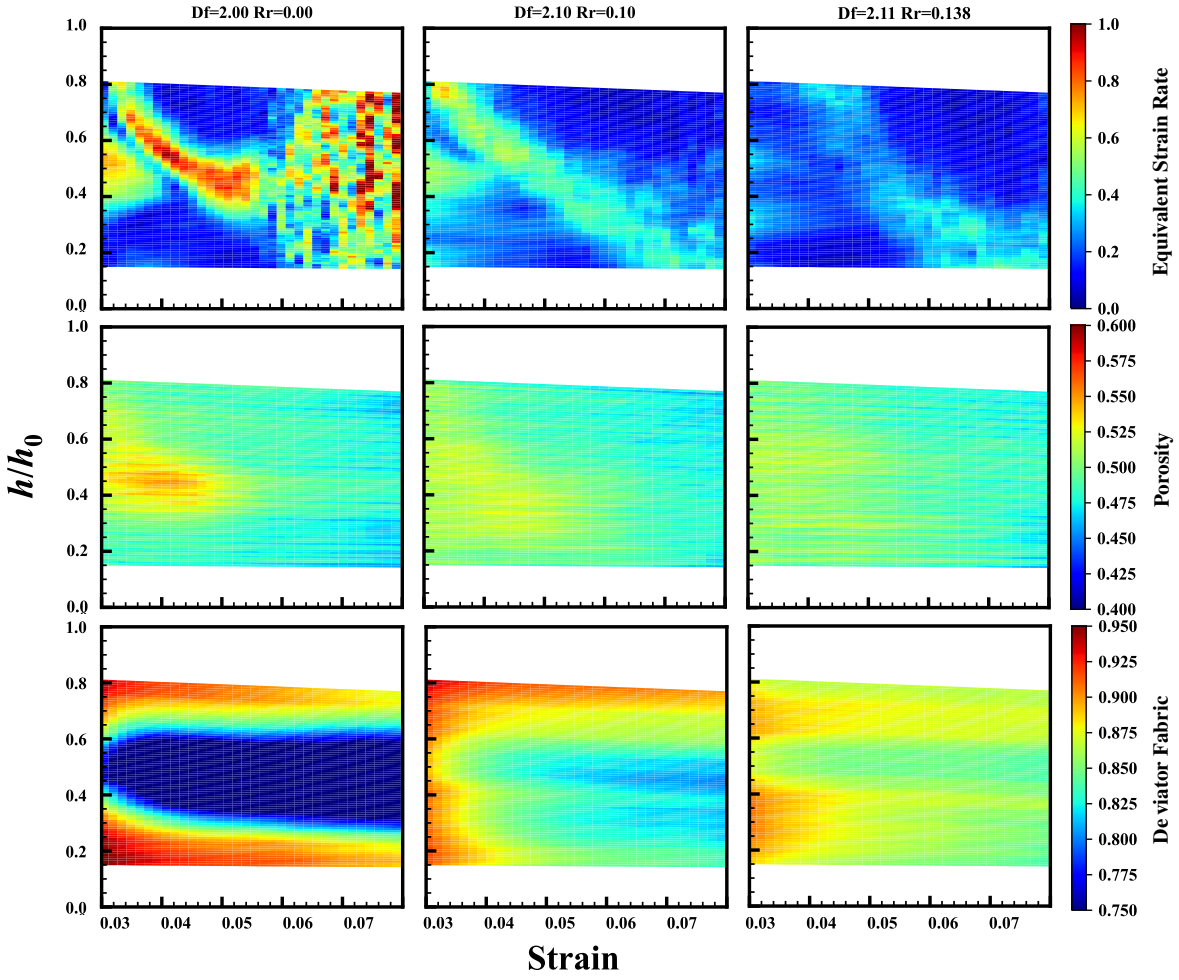

FIGURE 4.1: Evolution of the strain rate, porosity, and particle orientation fabric with respect to vertical strain in virtual packings of spheres ($D_f = 2.00$, $R_r = 0.00$) and two irregular morphologies($D_f = 2.10$, $R_r = 0.10$ and $D_f = 2.11$, $R_r = 0.138$). Patterns indicating strain localisation occur for the irregular particles.

Figure 4.1 presents the compaction-induced evolution of equivalent strain rate, porosity, and particle orientation fabric for three particle assemblies that consist of smooth or rough particles. The deformation behaviour of the smooth spherical particle model ($D_f = 2.00$, $R_r = 0.00$) is fundamentally different compared to the models with rough irregular particles ($D_f = 2.10$, $R_r = 0.10$ and $D_f = 2.11$, $R_r = 0.138$).

For the sphere assembly, the strain rate diagram in Figure 4.1 shows a sharp transition between two deformation modes - from local consolidation at the start of uniaxial loading (since strain = 0.03) to homogeneous deformation throughout the sample at higher strains. Following the transition, the porosity distributes evenly throughout the sample, confirming the consolidated state characterised by homogeneous deformation. During uniaxial compression, the deviator value of the particle orientation fabric drops dramatically, depicting minimal preferred particle orientation.

Compared to the sphere assembly, the models with irregular particles display little sign of consolidation in the strain rate diagrams in Figure 4.1. At the start of uniaxial loading approaching strain = 0.03, a highlight band initiates at the top boundary and propagates downwards until it reflects upwards near the bottom boundary. This pattern is similar to that of compaction band propagation, such as in the work of Blatny et al. (2022). Marketos and Bolton (2009) demonstrated the mechanism of compaction band propagation in numerical systems, showing how stress concentration at the band tip drives continued propagation. Following the principal stress trajectory, the compaction band advances through the progressive relaxation of geometric constraints, layer by layer. Each increment of compaction locally unlocks kinematic constraints in the adjacent material, creating a void in the strong-force network at the band tip. Band reflection occurs through similar stress redistribution mechanisms (Barraclough et al., 2017).

Moreover, the two models with different irregular particle morphologies yield distinct strain rate diagrams in Figure 4.1. The $D_f = 2.10$ $R_r = 0.10$ model exhibits clearer band boundaries, while the $D_f = 2.11$ $R_r = 0.138$ model shows more diffuse patterns. The starting point and the inclination of the band also differ in the strain rate diagrams. These differences suggest shape-dependence in the formation and propagation of compaction bands. To further investigate the effect of particle shape on compaction band formation and propagation in granular materials, the two SH shape parameters R_r and D_f were controlled separately in DEM simulations, whose evolution diagrams are presented in Figure 4.2 and Figure 4.3, respectively.

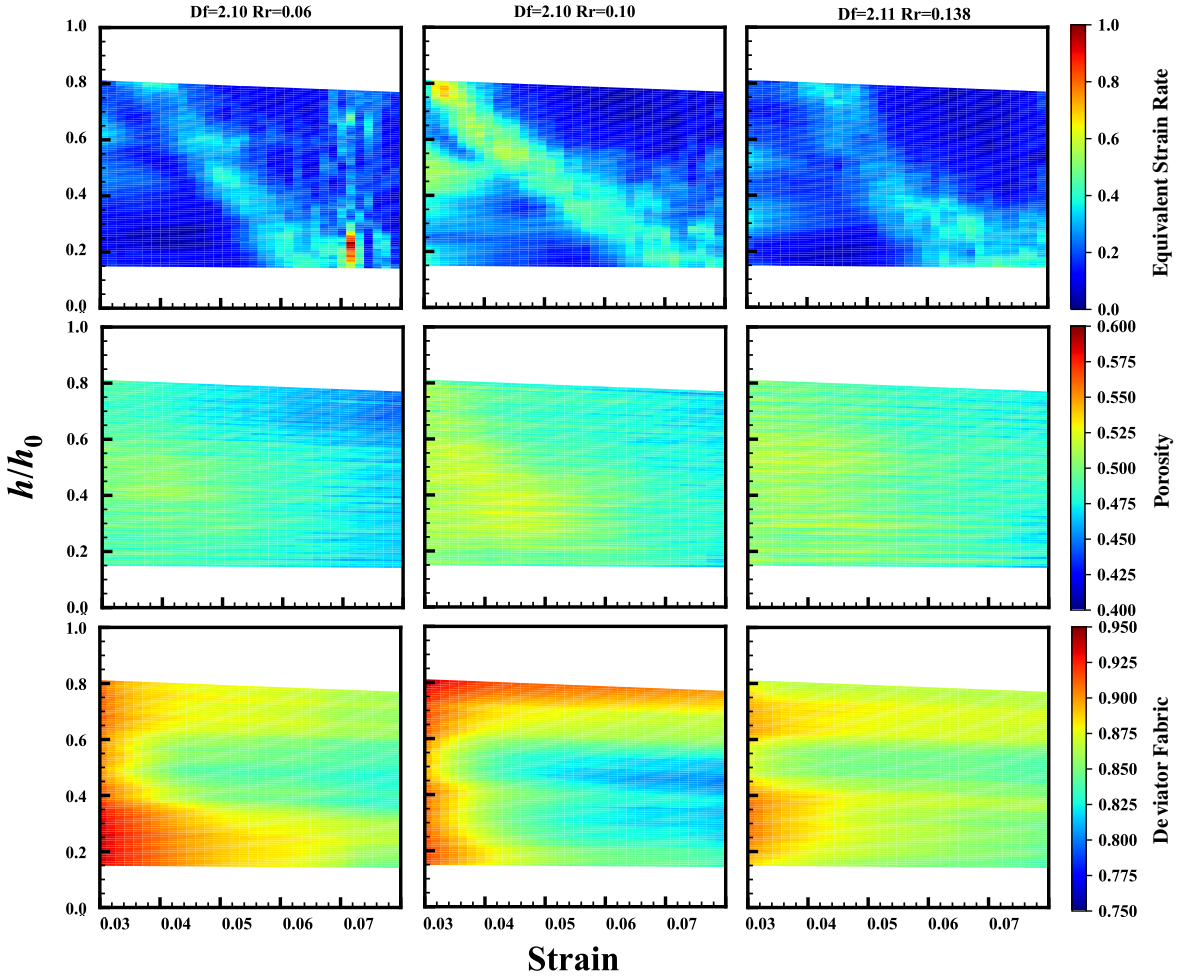

FIGURE 4.2: Evolution of the strain rate, porosity, and particle orientation fabric with respect to vertical strain in virtual packings of irregular particles, where the fractal dimension D_f is controlled and the relative roughness R_r is varied. Patterns indicating strain localisation are the strongest in the model with particle morphology specifications $D_f = 2.10$ and $R_r = 0.10$.

4.1.2 Effect of particle surface roughness

Figure 4.2 examines the effect of particle surface roughness R_r on compaction band formation while maintaining a roughly constant fractal dimension ($D_f \approx 2.10$). The porosity diagrams of three R_r values show a slight suppression of porosity during compaction from initially consolidated states. Similar to the diagrams in Figure 4.1, the strain rate diagrams here exhibit different highlight band characteristics, and the deviator fabric diagrams show different evolution of particle orientation, due to differences in the particle morphology. From $R_r = 0.06$ to 0.10, the highlight band forms earlier, propagates downwards more slowly, and presents more clearly. From $R_r = 0.10$ to 0.138, the highlight band forms later, propagates downwards faster, following a non-linear path, and is more diffused. Note that the reverted

trend at higher roughness occurs with reduced initial particle alignment, as indicated by the lower initial deviator fabric.

Particle surface roughness enhances friction at interlocking contacts. The smooth sphere model shows no compaction band through Figure 4.1. While keeping the particles well-aligned before compression, as in the models with $R_r = 0.06$ or 0.10, Figure 4.2 depicts enhancing compaction band patterns due to increasing particle surface roughness R_r. These figures suggest that friction may act as the selection mechanism determining the onset of localisation. In particle assemblies with fractal particle shapes, the transition from distributed deformation to localised deformation occurs when the former becomes energetically unfavourable due to increasing particle interlocking. In loose packings or assemblies with low inter-particle friction, there is little rolling and sliding resistance between particles, allowing them to rearrange homogeneously under load, as in the smooth sphere model in Figure 4.1. In dense packings with the friction and fractal geometry, the granular skeleton resists deformation due to particle interlocking until local frictional sliding happens, as in the rough models in Figure 4.2.

4.1.3 Effect of particle fractal dimension

Figure 4.3 illustrates the influence of fractal dimension D_f while maintaining a constant relative roughness ($R_r = 0.10$). The even colour at a vertical strain of 0.03 in the porosity diagrams indicates that the granular materials are initially consolidated due to previous isotropic confinement. In the strain rate diagrams, the highlight band initiates later and propagates downwards faster in particle assemblies with higher D_f, with little differences in the clarity of the band. Baud et al. (2004) investigated the propagation of the fracture-induced compaction band in Bentheim sandstone, and observed rapid propagation of compaction bands once initiated. They attribute it to a cascading failure mechanism where grain crushing creates local force redistribution onto neighbouring grains, triggering rapid band propagation through sequential collapse. Chen et al. (2024) confirmed that angular particles create a more intense contact network, which would set the stage for greater mechanical contrast. As indicated by the persistence of the red band in the deviator fabric diagrams in Figure 4.3, the interlock between particles is tighter in models with higher D_f, causing faster band propagation due to greater mechanical contrast in the granular material.

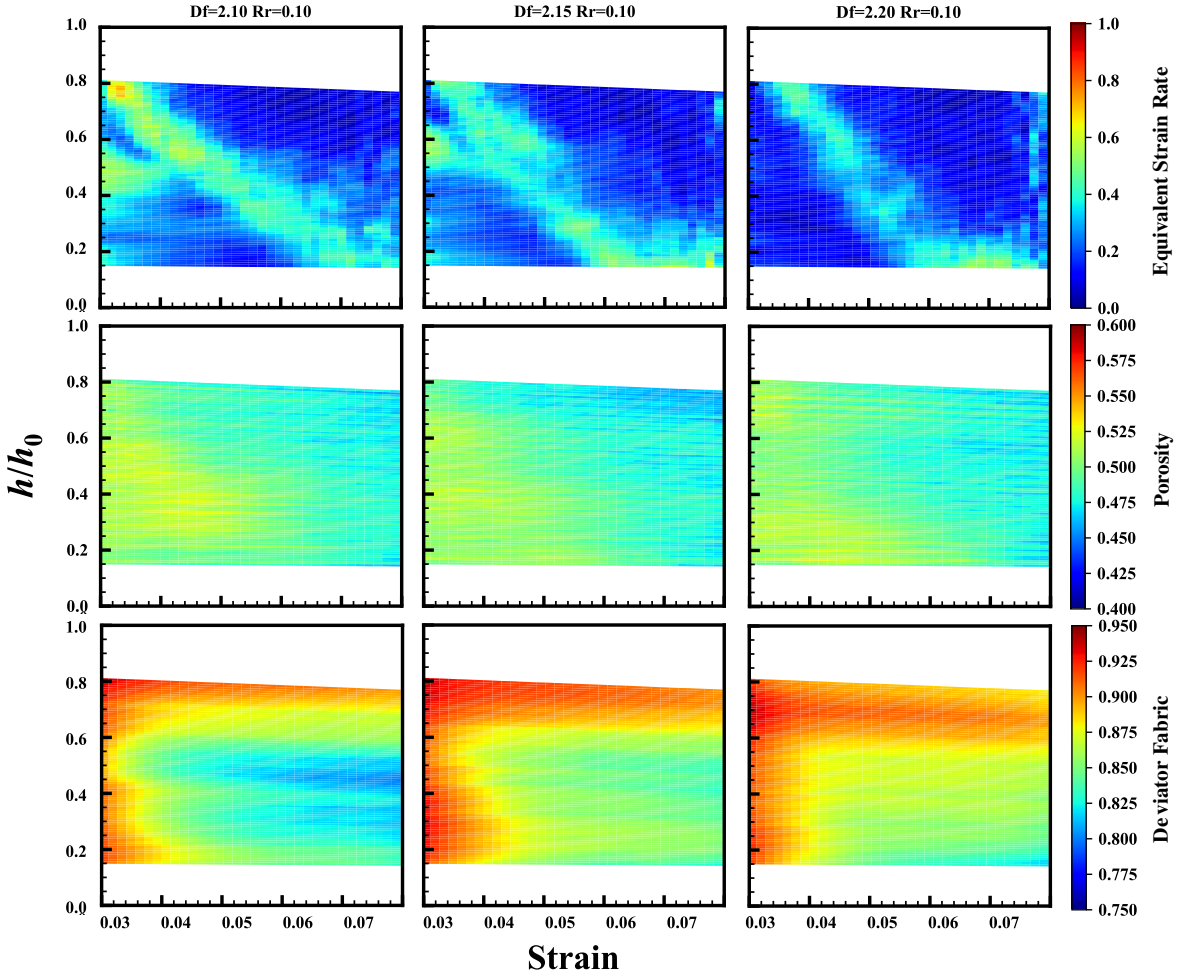

FIGURE 4.3: Evolution of the strain rate, porosity, and particle orientation fabric with respect to vertical strain in virtual packings of irregular particles, where the relative roughness R_r is controlled and the fractal dimension D_f is varied. With increasing D_f, the light band in the strain rate diagrams becomes narrower and propagates downwards faster, and the deviator fabric of particle orientation persists to remain red as kipping anisotropy.

4.1.4 Selecting representative elementary volumes for pore-space analysis

Patterns resembling compaction bands are observed in the evolution diagrams for DEM simulations with irregular particle assembly, where the porosity resists changes in dense packings. The patterns are shape-dependent. When the initial fabric is well-aligned, strain rate diagrams show clearer bands with higher particle surface roughness R_r, and the bands initiate later and propagate faster with higher particle fractal dimension D_f.

Previous experimental studies have shown that permeability evolves during compactive strain localisation in oedometer tests, as fabric changes through breakage-induced pore collapse

and microcrack formation. In the current study, particle breakage is suppressed in the DEM simulations, yet compaction bands still form due to stick-slip at particle contacts. In the absence of particle breakage, the pore space collapses less and its orientation exhibits a lower degree of anisotropy compared to that of the particle orientation.

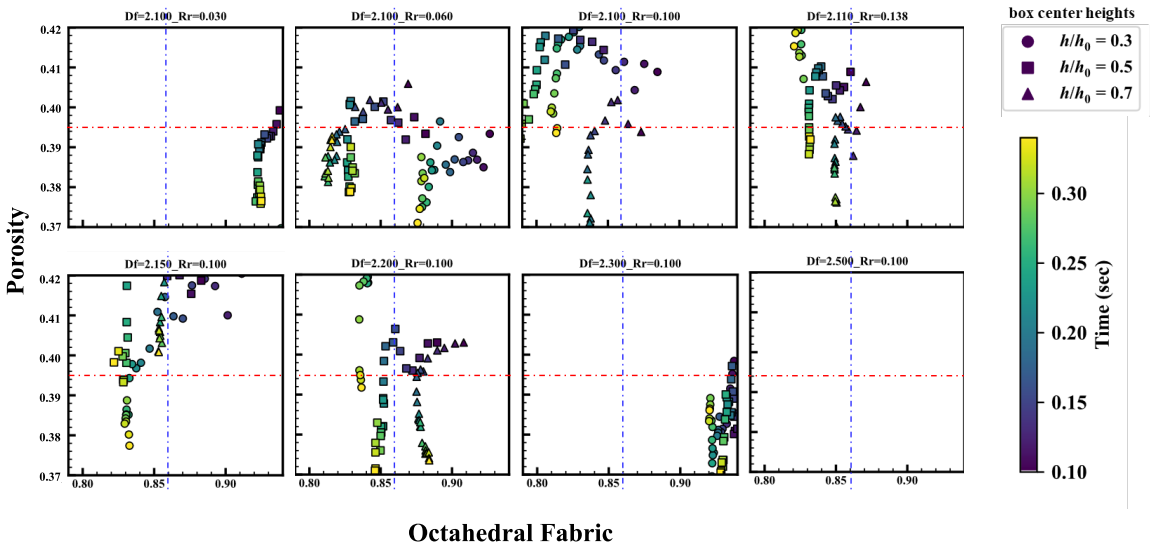

FIGURE 4.4: REV and time selection based on estimated porosity and particle orientation fabric.

To further investigate the influence of particle morphology on the pore-space anisotropy, REVs were selected from DEM simulations with various particle morphologies at specific heights and loading strains. For each REV, the pore orientation fabric is quantified, and the permeability in three orthogonal directions is estimated. Figure 4.4 was created using the estimated porosity (based on the total volume of particles) and the particle orientation fabric. A selection of cases in different combinations of D_f and R_r is presented in the figure. The horizontal axis indicates the deviator value of particle orientation fabric, and the vertical axis depicts the estimated porosity. The horizontal and vertical axes are uniformly scaled to the same range across different cases. These plots show varying evolution paths of the porosity and fabric anisotropy at different REV box heights. We targeted a porosity of 0.395 (red dashed lines) and a deviator fabric of 0.86 (blue dashed lines) to select REVs from crossover heights and time values. There may be no crossovers within the range in some cases, such as the last in Figure 4.4; they are excluded from the permeability calculation.

4.2 Evolution of the porosity, pore orientation fabric, and permeability

In this section, we present pore-space measurements within REVs from DEM simulations with different particle morphologies at specific heights and loading strains. We focus on the degree of anisotropy in the pore orientation fabric and permeability. In Section 4.2.1, we present the evolution of the porosity and pore orientation fabric in boxes at three heights throughout the compressive loading stage, and we discuss the effect of particle morphology herein. In Section 4.2.2, the result depicts the consistent preferential flow direction through the selected REVs along the loading direction, and we evaluated the degree of anisotropy in permeability against particle shapes. In Section 4.2.3, we attempt to correlate pore orientation fabric and permeability anisotropy, and to discuss the influence of particle shape on permeability anisotropy via the evolution of the pore structure during strain localisation.

4.2.1 The porosity and pore orientation fabric

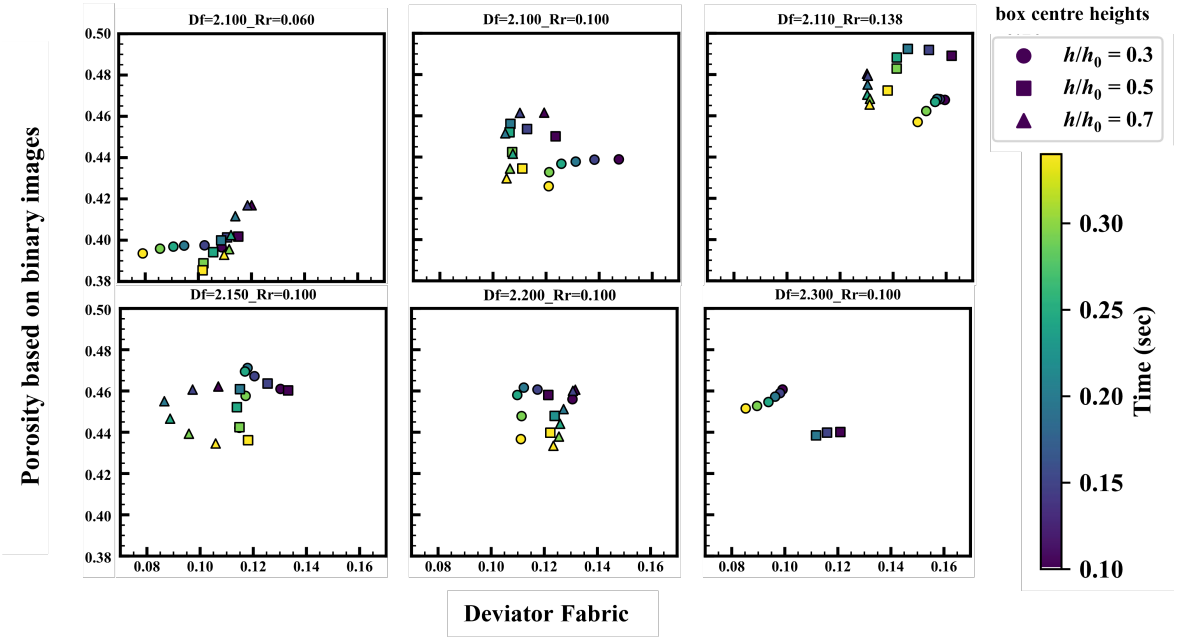

FIGURE 4.5: Evolution of the porosity and pore orientation fabric in boxes at three heights during compression. The boxes are in the same size as the selected REVs. Only the time during the loading stage is included, from the start of uniaxial compression at 0.10 sec to the subsequent deformation at 0.35 sec, with an increment of 0.05 sec.

Virtual packings in DEM were isotropically confined from uniformly placed particles on rigid points, as demonstrated in Chapter 3. Although the same porosity was targeted at the end of the confinement, models exhibit slight differences in porosity due to varying particle shapes, as depicted in Figure 4.5, which shows varying patterns in the evolution of the porosity and pore orientation fabric during the vertical compression. In the presented plots for six particle morphology settings, the porosity and pore orientation anisotropy mainly decrease during the compaction process, with the latter showing more exceptions and inverse trends. The evolution of the porosity and pore orientation fabric differs at different REV box heights. This difference suggests that the virtual granular assembly is heterogeneous and deforms differently over the height.

Due to heterogeneity in the virtual granular assembly, the strength of inter-particle frictional contacts may become stronger at particular heights during compaction. Occasionally, the alteration of porosity or deviator fabric may become more energetically preferable than another, leading to the turns in the evolution paths in Figure 4.5.

To compare the evolution between different particle morphologies, the x- and y- axes in Figure 4.5 are unified. Data points outside the x- and y- ranges are cropped out, such as the triangles representing the REV at $h/h_0 = 0.7$ from the DEM simulation of particle morphology $D_f = 2.300$ and $R_r = 0.100$.

The three plots on the top row represent morphologies with increasing R_r and similar D_f from left to right, where the data scatter shifts toward the top-right direction. Particles with higher roughness build stronger interlocking at contacts, and form more rigid granular skeletons that are resistant to rotation and deformation (Chen et al., 2024). As a result, even with the same fractal dimension, models with higher grain surface roughness exhibit higher initial pore-scale fabric anisotropy (depicted by higher deviator fabric) and porosity.

As indicated by Figure 4.3, compaction band occurs in the three models with the same relative roughness ($R_r = 0.100$) and different fractal dimensions ($D_f = 2.100, 2.150, 2.200$). These models show comparable ranges of pore orientation fabric and porosity evolution during compression, suggesting a minor direct effect of the fractal dimension on pore-structure anisotropy.

4.2.2 Effect of particle morphology on the permeability anisotropy

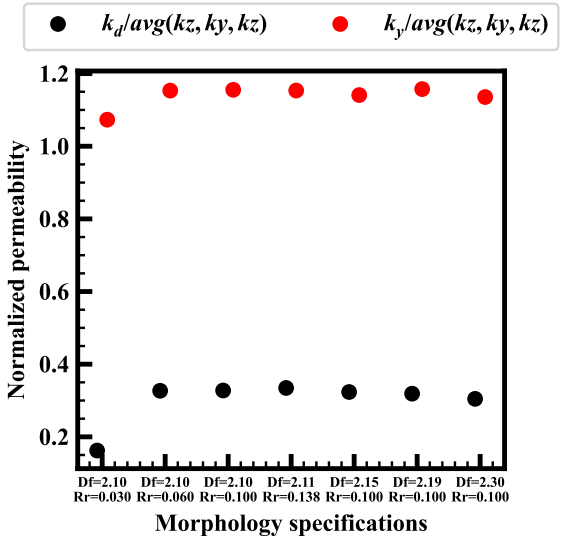

FIGURE 4.6: Permeability in Y-direction and the deviator value normalised by the overall average of k_x, k_y, and k_z, with respect to different morphology specifications. Each value is averaged from all CFD simulations sharing the same morphology specification of D_f and R_r.

The permeability was estimated within the selected REVs at three heights in X-, Y-, and Z- directions as k_x, k_y, and k_z, respectively. And the degree of permeability anisotropy k_d was determined following Equation 3.21. The REVs exhibit slight variations in porosity. To highlight the permeability anisotropy, the dominating effect of porosity on permeability is suppressed via dividing k_y and k_d by the average value of k_x, k_y, and k_z. To focus on the effect of particle morphology on permeability anisotropy, k_y and k_d are further averaged over the same D_f and R_r combination, yielding single values of k_y/k_{avg} and k_d/k_{avg} for each shape specification, where $k_{\text{avg}} = (k_x + k_y + k_z)/3$. These values are presented in Figure 4.6. All CFD simulations show the highest permeability values in the Y-direction, resulting in all k_y/k_{avg} values exceeding 1.0. This demonstrates that pore networks are suppressed perpendicular to the principal compressive stress, both within and outside localisation zones.

Both quantities in Figure 4.6 vary similarly with respect to the morphology. The normalised values are comparable for REVs containing rough particles with $R_r \geq 0.060$ and lower values where the particles are less rough with $R_r = 0.030$. Note that the DEM model with $R_r = 0.030$ shows no clear sign of compaction bands, which are present in models with higher R_r. The matching pattern of the absence of the compaction band and the lower values of normalised permeability suggests that permeability anisotropy occurs in granular assemblies

with rough particle surfaces through compaction band formation, while the direct influence of particle morphology on the degree of anisotropy is insignificant.

4.2.3 Relationship between the pore orientation fabric and permeability anisotropy

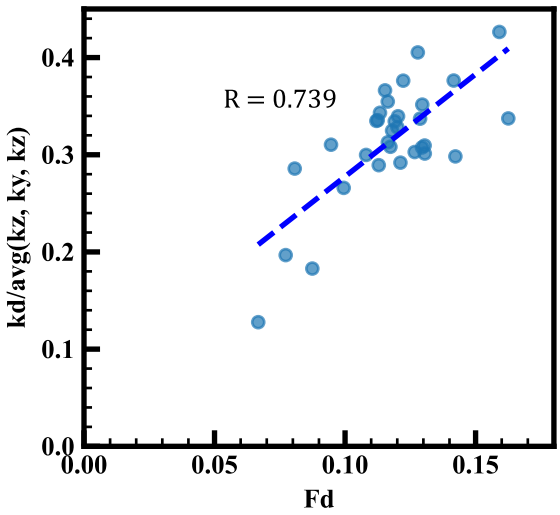

FIGURE 4.7: Correlation between the permeability anisotropy characterised by k_d/k_{avg} ($k_{\text{avg}} = \text{avg}(k_x, k_y, k_z)$) and the deviator value F_d of pore orientation fabric representing the fabric anisotropy.

To investigate the effect of the pore orientation fabric on permeability anisotropy, F_d representing the former and k_d/k_{avg} indicating the latter were correlated, as shown in Figure 4.7. Based on the ACF analysis of the voxelised pore-space in each REV, a 3×3 fabric tensor Φ_{ij} was determined, which is thereby implemented in Equation 3.13 to calculate $F_d = \Phi_d$ as the deviator value indicating the anisotropy in pore orientation fabric. The strong correlation ($R = 0.739$) suggests that the preferential pore alignment is associated with the permeability anisotropy. Heap et al. (2024) made similar observations that the preferred pocket (pore) orientation in deformed olivine aggregate induces anisotropic permeability. Previous experiments on particle breakage during compaction band formation also indicated enhanced permeability along the direction of microcracks (Zhu et al., 1997), which are pores at the micro-scale induced by particle breakage during compaction.

Permeability anisotropy may also be attributed to direction-dependent tortuosity (Heap et al., 2024), which may evolve differently during deformation under varying particle shapes and loading conditions (Cabalar & Hasan, 2013). Zhao and O'Sullivan (2022) suggested that

more angular particles generate a more complex pore topology, which influences bulk flow tortuosity more significantly than particle angularity. While permeability anisotropy is directly associated with pore orientation at an intermediate scale, it is primarily influenced by pore connectivity at a larger scale (Bader et al., 2024).

4.3 Summary

The results collectively demonstrate that particle shape influences permeability anisotropy primarily by altering the pore orientation fabric in relation to compaction band formation. Rough particles enable strain localisation in granular materials during compression via frictional stick-slip contact behaviours, and particles with higher fractal dimensions cause delayed formation and fast propagation of compaction bands due to stronger interlocking at inter-particle contacts. Due to the absence of particle breakage in the DEM simulations, the compaction bands here do not yield a significant reduction in porosity. The initial pore orientation fabric right after confinement depends on the surface roughness R_r of the particles in the DEM simulations, while the pore orientation fabric becomes slightly less anisotropic during compression regardless of particle shapes. By averaging permeability estimates for REVs with the same particle morphology parameters and suppressing randomness in pore networks, the direct effect of particle morphology on permeability anisotropy is found to be insignificant.

CHAPTER 5

Conclusions and future work

5.1 Conclusions

In this thesis, the effect of particle morphology on the evolution of the fabric and the permeability during compaction has been numerically investigated using discrete element modelling (DEM) and computational fluid dynamics (CFD) with two main aims: (i) to observe the deformation patterns of dense granular media without particle breakage, and (ii) to systematically assess the effect of particle morphology on the evolution of both fabric and permeability during compression. The insights gained from this study are summarised below:

- Strain localisation in the form of compaction bands can develop through frictional stick-slip mechanisms at interlocked particle contacts without particle breakage.
- More irregular particles (with a higher fractal dimension D_f) exhibit faster compaction band propagation rates, with the bands initiating later but advancing more rapidly through the granular assembly compared to rounder particles.
- The largest permeability consistently occurs along the loading direction in strain localisation zones, perpendicular to the direction of pore collapse.
- Permeability anisotropy develops primarily in granular assemblies with rough particle surfaces ($R_r \geq 0.060$) through the formation of compaction bands, while smoother particles show more homogeneous deformation with reduced anisotropy in fabric and permeability.
- While particle roughness triggers anisotropic behaviour, the degree of permeability anisotropy shows no significant direct relationship with particle morphology, while a

compaction band is present. Particle morphology primarily influences permeability anisotropy by altering the pore orientation fabric and tortuosity.

5.2 Future work

The computational frameworks and findings presented in this thesis offer practical tools for understanding strain localisation in granular materials where particle breakage is minimal or absent. Researchers can use dense granular assemblies with rough particles to investigate particle-scale mechanisms while expecting the presence of a compaction band. The DEM-LBM workflow establishes a methodology for quantifying the evolution of the fabric and permeability during granular deformation.

The main contribution of this study was to reveal the effect of particle surface roughness on the formation of compaction bands and the induction of permeability anisotropy. The results obtained from this work give rise to the following hypotheses regarding the incorporation of particle breakage in future studies:

Inversion of Propagation Dynamics: The introduction of particle breakage will likely invert the propagation dynamics observed in rigid-confinement simulations. The thesis revealed faster compaction band propagation with more angular particles due to enhanced interlocking, where angular tips on particle surfaces create a stiff skeleton in stress transmission. However, in a breakage-enabled scenario, these same angular tips may comminute locally due to stress concentration. The comminution could dissipate the strain energy and prevent propagation. Consequently, the currently observed association between faster band propagation and higher particle angularity may be less pronounced or even reversed if particle breakage is enabled.

Stagnation of Band Propagation: A similar reversal is expected regarding boundary mechanics. The band reflection observed in the current results is a specific consequence of the elastic conservation of energy; when the band impacts the rigid bottom boundary, the energy must rebound. In a general scenario, the rigid boundary represents a zone of infinite stiffness contrast where local contact stresses will spike drastically. If the particle strength is exceeded, this stress concentration may trigger pulverization at the boundary to dissipate kinetic energy, leading to the stagnation of compaction band once it hits the bottom boundary.

Decoupling of Hydraulic Anisotropy: The strong linear correlation between pore orientation fabric and permeability anisotropy established in this thesis relies on the preservation of the primary pore network. The fines generated by crushing will migrate into and clog the pore throats, increase geometric tortuosity, and reduce pore connectivity. Even if fines migrate along preferential flow directions, this would disproportionately clog the dominant pathways that originally created the anisotropy, thereby reducing the permeability differential between directions. While the structural fabric of the granular material may remain anisotropic due to the alignment of surviving large grains, the hydraulic anisotropy will decouple, tending towards isotropy as fines block flow paths in all directions.

Bibliography

Al-Raoush, R. (2007). Microstructure characterization of granular materials. *Physica A: Statistical mechanics and its Applications*, *377*(2), 545–558.

Altuhafi, F., & COOP, M. R. (2011). Changes to particle characteristics associated with the compression of sands. *Géotechnique*, *61*(6), 459–471.

Ansys. (2024). Contact detection [Ansys Rocky Technical Manual, Release 2024 R2].

Askey, R. (2005). The 1839 paper on permutations: Its relation to the Rodrigues formula and further developments. *Mathematics and Social Utopias in France: Olinde Rodrigues and His Times*, *28*, 105–118.

Bader, J., Zhu, W., Montési, L., Qi, C., Cordonnier, B., Kohlstedt, D., & Warren, J. (2024). Effects of stress-driven melt segregation on melt orientation, melt connectivity and anisotropic permeability. *Journal of Geophysical Research: Solid Earth*, *129*(3), e2023JB028065.

Barraclough, T. W., Blackford, J. R., Liebenstein, S., Sandfeld, S., Stratford, T. J., Weinländer, G., & Zaiser, M. (2017). Propagating compaction bands in confined compression of snow. *Nature Physics*, *13*(3), 272–275.

Barreto, D., O'Sullivan, C., & Zdravkovic, L. (2009). Quantifying the evolution of soil fabric under different stress paths. *AIP conference proceedings*, *1145*, 181–184.

Batchelor, G. K. (2000). *An introduction to fluid dynamics*. Cambridge university press.

Baud, P., Klein, E., & Wong, T.-f. (2004). Compaction localization in porous sandstones: Spatial evolution of damage and acoustic emission activity. *Journal of Structural Geology*, *26*(4), 603–624.

Baud, P., Meredith, P., & Townend, E. (2012). Permeability evolution during triaxial compaction of an anisotropic porous sandstone. *Journal of Geophysical Research: Solid Earth*, *117*(B5).

Beucher, S., & Meyer, F. (2018). The morphological approach to segmentation: The watershed transformation. In *Mathematical morphology in image processing* (pp. 433–481). CRC Press.

Blatny, L., Berclaz, P., Guillard, F., Einav, I., & Gaume, J. (2022). Microstructural origin of propagating compaction patterns in porous media. *Physical Review Letters*, *128*(22), 228002.

Brinkman, H. C. (1949). A calculation of the viscous force exerted by a flowing fluid on a dense swarm of particles. *Flow, Turbulence and Combustion*, *1*(1), 27–34.

Cabalar, A., & Hasan, R. (2013). Compressional behaviour of various size/shape sand–clay mixtures with different pore fluids. *Engineering Geology*, *164*, 36–49.

Carman, P. C. (1939). Permeability of saturated sands, soils and clays. *The Journal of Agricultural Science*, *29*(2), 262–273.

Carman, P. C. (1956). *Flow of gases through porous media*. Academic Press; Butterworths.

Carrier III, W. D. (2003). Goodbye, Hazen; hello, Kozeny-Carman. *Journal of geotechnical and geoenvironmental engineering*, *129*(11), 1054–1056.

Casagrande, A. (1944). Shear failure of anisotropic materials. *Proc. Boston Soc. Civ. Engrs*, *31*, 74–87.

Chapuis, R. P. (2004). Predicting the saturated hydraulic conductivity of sand and gravel using effective diameter and void ratio. *Canadian geotechnical journal*, *41*(5), 787–795.

Chen, J., Zhao, C., Chen, Y., & Yang, Z. (2024). Effects of particle overall regularity and surface roughness on fabric evolution of granular materials: DEM simulations. *International Journal for Numerical and Analytical Methods in Geomechanics*, *48*(13), 3284–3307.

Cheung, C. S., Baud, P., & Wong, T.-f. (2012). Effect of grain size distribution on the development of compaction localization in porous sandstone. *Geophysical Research Letters*, *39*(21).

Cho, G.-C., Dodds, J., & Santamarina, J. C. (2006). Particle shape effects on packing density, stiffness, and strength: Natural and crushed sands. *Journal of geotechnical and geoenvironmental engineering*, *132*(5), 591–602.

Chork, C., Jian, F., & Taggart, I. (1994). Porosity and permeability estimation based on segmented well log data. *Journal of Petroleum Science and Engineering*, *11*(3), 227–239.

Cline, H. E., Dumoulin, C., Hart Jr, H., Lorensen, W. E., & Ludke, S. (1987). 3D reconstruction of the brain from magnetic resonance images using a connectivity algorithm. *Magnetic Resonance Imaging*, *5*(5), 345–352.

Cundall, P. A., & Strack, O. D. (1979). A discrete numerical model for granular assemblies. *geotechnique*, *29*(1), 47–65.

Deng, S., Zuo, L., Aydin, A., Dvorkin, J., & Mukerji, T. (2015). Permeability characterization of natural compaction bands using core flooding experiments and three-dimensional image-based analysis: Comparing and contrasting the results from two different methods. *Aapg Bulletin*, *99*(1), 27–49.

Druckrey, A. M., Alshibli, K. A., & Al-Raoush, R. I. (2016). 3D characterization of sand particle-to-particle contact and morphology. *Computers and Geotechnics*, *74*, 26–35.

Fernlund, J. M. (1998). The effect of particle form on sieve analysis: A test by image analysis. *Engineering Geology*, *50*(1-2), 111–124.

Fonseca, J., O'Sullivan, C., & Coop, M. R. (2009). Image Segmentation Techniques for Granular Materials. *AIP Conference Proceedings*, *1145*(1), 223–226.

Fonseca, J., O'sullivan, C., Coop, M., & Lee, P. (2013). Quantifying the evolution of soil fabric during shearing using scalar parameters. *Géotechnique*, *63*(10), 818–829.

Fonseca, J. (2011). *The evolution of morphology and fabric of a sand during shearing* [Doctoral dissertation, Imperial College London].

Forchheimer, P. (1901). Wasserbewegung. *Ver. Dtsch. Ing.*, *45*, 1782–1788.

Formware. (2025). Online STL Repair Tool [Accessed: 2025-10-09].

Fu, P., & Dafalias, Y. F. (2015). Relationship between void- and contact normal-based fabric tensors for 2D idealized granular materials. *International Journal of Solids and Structures*, *63*, 68–81.

Garcia, X., Akanji, L. T., Blunt, M. J., Matthai, S. K., & Latham, J. P. (2009). Numerical study of the effects of particle shape and polydispersity on permeability. *Physical Review E—Statistical, Nonlinear, and Soft Matter Physics*, *80*(2), 021304.

Gerig, G., Styner, M., Jones, D., Weinberger, D., & Lieberman, J. (2001). Shape analysis of brain ventricles using SPHARM. *Proceedings IEEE workshop on mathematical methods in biomedical image analysis (MMBIA 2001)*, 171–178.

Guillard, F., Golshan, P., Shen, L., Valdes, J. R., & Einav, I. (2015). Dynamic patterns of compaction in brittle porous media. *Nature Physics*, *11*(10), 835–838.

Guo, P., & Su, X. (2007). Shear strength, interparticle locking, and dilatancy of granular materials. *Canadian Geotechnical Journal*, *44*(5), 579–591.

Hassanizadeh, M., & Gray, W. G. (1980). General conservation equations for multi-phase systems: 3. constitutive theory for porous media flow. *Advances in water resources*, *3*(1), 25–40.

Hazen, A. (1892). Some physical properties of sands and gravels. mass. state board of health. *24th Annual Report*, 539–556.

Hazen, A. (1911). Discussion of "dams on sand foundations" by A. C. Koenig. *Trans. Am. Soc. Civ. Eng.*, *73*, 199–203.

Heap, M. J., Bayramov, K., Meyer, G. G., Violay, M. E., Reuschlé, T., Baud, P., Gilg, H. A., Harnett, C. E., Kushnir, A. R., Lazari, F., et al. (2024). Compaction and permeability evolution of tuffs from Krafla volcano (Iceland). *Journal of Geophysical Research: Solid Earth*, *129*(8), e2024JB029067.

Heap, M. J., Brantut, N., Baud, P., & Meredith, P. G. (2015). Time-dependent compaction band formation in sandstone. *Journal of Geophysical Research: Solid Earth*, *120*(7), 4808–4830.

Holcomb, D., & Olsson, W. (2003). Compaction localization and fluid flow. *Journal of Geophysical Research: Solid Earth*, *108*(B6).

Holtz, R. D., Kovacs, W. D., & Sheahan, T. C. (1981). *An introduction to geotechnical engineering* (Vol. 733). Prentice-Hall.

Huffine, C. L., & Bonilla, C. F. (1962). Particle-size effects in the compression of powders. *American Institute of Chemical Engineers Journal*, *8*(4), 490–493.

Issen, K. A., & Rudnicki, J. W. (2001). Theory of compaction bands in porous rock. *Physics and Chemistry of the Earth, Part A: Solid Earth and Geodesy*, *26*(1), 95–100.

Iwashita, K., & Oda, M. (2020). *Mechanics of granular materials: An introduction*. CRC press.

Iwashita, K., & Oda, M. (2000). Micro-deformation mechanism of shear banding process based on modified distinct element method. *Powder Technology*, *109*(1), 192–205.

Jiang, M. J., Yu, H. S., & Harris, D. (2005). A novel discrete model for granular material incorporating rolling resistance. *Computers and Geotechnics*, *32*(5), 340–357.

Keller, L., & Holzer, L. (2018). Image-based upscaling of permeability in Opalinus clay. *Journal of Geophysical Research: Solid Earth*, *123*(1), 285–295.

Kerimov, A., Mavko, G., Mukerji, T., Dvorkin, J., & Al Ibrahim, M. A. (2018). The influence of convex particles' irregular shape and varying size on porosity, permeability, and

elastic bulk modulus of granular porous media: Insights from numerical simulations. *Journal of Geophysical Research: Solid Earth*, *123*(12), 10–563.

Kozeny, J. (1927). Ueber kapillare leitung des wassers im boden. *Sitzungsberichte der Akademie der Wissenschaften in Wien*, *136*, 271.

Krumbein, W., & Sloss, L. (1963). *Stratigraphy and sedimentation*. W.H. Freeman.

Kuhn, M. R., Sun, W., & Wang, Q. (2015). Stress-induced anisotropy in granular materials: Fabric, stiffness, and permeability. *Acta Geotechnica*, *10*, 399–419.

Kuo, C.-Y., Frost, J. D., & Chameau, J. (1998). Image analysis determination of stereology based fabric tensors. *Geotechnique*, *48*(4), 515–525.

Li, J., & Gu, Y. (2005). Coalescence of oil-in-water emulsions in fibrous and granular beds. *Separation and purification technology*, *42*(1), 1–13.

Lindblad, J. (2005). Surface area estimation of digitized 3D objects using weighted local configurations. *Image and Vision Computing*, *23*(2), 111–122.

Marketos, G., & Bolton, M. (2009). Compaction bands simulated in discrete element models. *Journal of structural Geology*, *31*(5), 479–490.

Mathavan, G., & Viraraghavan, T. (1992). Coalescence/filtration of an oil-in-water emulsion in a peat bed. *Water Research*, *26*(1), 91–98.

Miller, K. J., Zhu, W.-l., Montési, L. G., & Gaetani, G. A. (2014). Experimental quantification of permeability of partially molten mantle rock. *Earth and Planetary Science Letters*, *388*, 273–282.

Mitchell, J. K., & Soga, K. (2005). *Fundamentals of soil behavior*. Wiley.

Miura, K., Maeda, K., Furukawa, M., & Toki, S. (1997). Physical characteristics of sands with different primary properties. *Soils and Foundations*, *37*(3), 53–64.

Mollema, P., & Antonellini, M. (1996). Compaction bands: A structural analog for anti-mode I cracks in aeolian sandstone. *Tectonophysics*, *267*(1-4), 209–228.

Morimoto, T., O'Sullivan, C., & Taborda, D. M. G. (2024). Linking sand permeability anisotropy to fabric anisotropy via numerical simulation. *E3S Web of Conferences*, *544*, 07004.

Nguyen, V. H., Gland, N., Dautriat, J., David, C., Wassermann, J., & Guelard, J. (2014). Compaction, permeability evolution and stress path effects in unconsolidated sand and weakly consolidated sandstone. *International Journal of Rock Mechanics and Mining Sciences*, *67*, 226–239.

Nie, J., Zhao, S., Cui, Y., & Wang, Y. (2022). Coupled effects of particle overall regularity and sliding friction on the shear behavior of uniformly graded dense sands. *Journal of Rock Mechanics and Geotechnical Engineering*, *14*(3), 873–885.

Oda, M. (1985). Permeability tensor for discontinuous rock masses. *Geotechnique*, *35*(4), 483–495.

Oda, M. (1972a). Initial fabrics and their relations to mechanical properties of granular material. *Soils and foundations*, *12*(1), 17–36.

Oda, M. (1972b). The mechanism of fabric changes during compressional deformation of sand. *Soils and foundations*, *12*(2), 1–18.

Oda, M. (1977). Co-ordination number and its relation to shear strength of granular material. *Soils and foundations*, *17*(2), 29–42.

Oda, M. (1982). Fabric tensor for discontinuous geological materials. *Soils and foundations*, *22*(4), 96–108.

Oda, M., Nemat-Nasser, S., & Konishi, J. (1985). Stress-induced anisotropy in granular masses. *Soils and foundations*, *25*(3), 85–97.

Olsson, W. A. (1999). Theoretical and experimental investigation of compaction bands in porous rock. *Journal of Geophysical Research: Solid Earth*, *104*(B4), 7219–7228.

O'Sullivan, C. (2011). *Particulate discrete element modelling: A geomechanics perspective*. CRC Press.

Press, W. H., Teukolsky, S. A., Vetterling, W. T., & Flannery, B. P. (1992). *Numerical recipes in C* (Vol. 2). Cambridge University Press.

Satake, M. (1982). Fabric tensor in granular materials. *IUTAM-Conference on Deformation and Failure of Granular Materials, 1982*, 63–68.

Suga, K., et al. (2015). A D3Q27 multiple-relaxation-time lattice Boltzmann method for turbulent flows. *Computers & Mathematics with Applications*, *69*(6), 518–529.

Sun, G., Zhang, Y., Sun, W., Liu, Z., & Wang, C. (2011). Multi-scale prediction of the effective chloride diffusion coefficient of concrete. *Construction and Building Materials*, *25*(10), 3820–3831.

Suo, S., Wei, D., Zhao, B., Zhai, C., & Gan, Y. (2024). On the drag coefficient universality of a rough grain in creeping flow. *arXiv preprint arXiv:2411.08225*.

Taylor, M. A. (2002). Quantitative measures for shape and size of particles. *Powder technology*, *124*(1-2), 94–100.

Thornton, C. (2000). Numerical simulations of deviatoric shear deformation of granular media. *Géotechnique*, *50*(1), 43–53.

Timm, K., Kusumaatmaja, H., Kuzmin, A., Shardt, O., Silva, G., & Viggen, E. (2016). The lattice Boltzmann method: Principles and practice. *Cham, Switzerland: Springer International Publishing AG*.

Tsomokos, A., & Georgiannou, V. (2010). Effect of grain shape and angularity on the undrained response of fine sands. *Canadian Geotechnical Journal*, *47*(5), 539–551.

Vajdova, V., Baud, P., & Wong, T.-f. (2004). Permeability evolution during localized deformation in Bentheim sandstone. *Journal of Geophysical Research: Solid Earth*, *109*(B10).

Valdes, J. R., Fernandes, F. L., & Einav, I. (2012). Periodic propagation of localized compaction in a brittle granular material. *Granular Matter*, *14*(1), 71–76.

Varga, P., & Zysset, P. (2009). Assessment of volume fraction and fabric in the distal radius using HR-pQCT. *Bone*, *45*(5), 909–917.

Varga, P., Pacureanu, A., Langer, M., Suhonen, H., Hesse, B., Grimal, Q., Cloetens, P., Raum, K., & Peyrin, F. (2013). Investigation of the three-dimensional orientation of mineralized collagen fibrils in human lamellar bone using synchrotron X-ray phase nano-tomography. *Acta biomaterialia*, *9*(9), 8118–8127.

Wadell, H. (1932). Volume, shape, and roundness of rock particles. *The Journal of Geology*, *40*(5), 443–451.

Wald, M. J., Vasilic, B., Saha, P. K., & Wehrli, F. W. (2005). Study of trabecular bone microstructure using spatial autocorrelation analysis. *Medical Imaging 2005: Physiology, Function, and Structure from Medical Images*, *5746*, 291–302.

Wang, G., Mitchell, T., Meredith, P., Nara, Y., & Wu, Z. (2016). Influence of gouge thickness and grain size on permeability of macrofractured basalt. *Journal of Geophysical Research: Solid Earth*, *121*(12), 8472–8487.

Wang, W., Wei, D., & Gan, Y. (2020). An experimental investigation on cemented sand particles using different loading paths: Failure modes and fabric quantifications. *Construction and Building Materials*, *258*, 119487.

Wang, X., Liang, Z., Nie, Z., & Gong, J. (2019). Stochastic numerical model of stone-based materials with realistic stone-inclusion features. *Construction and Building Materials*, *197*, 830–848.

Wei, D. (2021). *Granular mechanics across length scales: Contact, breakage, fracture, and permeability* [Doctoral dissertation, University of Sydney].

Wei, D., Wang, Z., Pereira, J.-M., & Gan, Y. (2021). Permeability of uniformly graded 3D printed granular media. *Geophysical Research Letters*, *48*, e2020GL090728.

Wei, D., Wang, J., Nie, J., & Zhou, B. (2018). Generation of realistic sand particles with fractal nature using an improved spherical harmonic analysis. *Computers and Geotechnics*, *104*, 1–12.

Wei, D., Zhao, B., Dias-da-Costa, D., & Gan, Y. (2019). An FDEM study of particle breakage under rotational point loading. *Engineering Fracture Mechanics*, *212*, 221–237.

Whitaker, S. (1969). Advances in theory of fluid motion in porous media. *Industrial & engineering chemistry*, *61*(12), 14–28.

Woodcock, N. (1977). Specification of fabric shapes using an eigenvalue method. *Geological Society of America Bulletin*, *88*(9), 1231–1236.

Wu, M., Wang, J., & Zhao, B. (2022). DEM modeling of one-dimensional compression of sands incorporating statistical particle fragmentation scheme. *Canadian Geotechnical Journal*, *59*(1), 144–157.

Yamamuro, J., & Wood, F. (2004). Effect of depositional method on the undrained behavior and microstructure of sand with silt. *Soil Dynamics and Earthquake Engineering*, *24*, 751–760.

Yang, J., & Luo, X. D. (2015). Exploring the relationship between critical state and particle shape for granular materials. *Journal of the Mechanics and Physics of Solids*, *84*, 196–213.

Yang, X. (2005). *Three-dimensional characterization of inherent and induced sand microstructure*. Georgia Institute of Technology.

Zeng, Z., & Grigg, R. (2006). A criterion for non-Darcy flow in porous media. *Transport in porous media*, *63*(1), 57–69.

Zhao, B., & O'Sullivan, C. (2022). Fluid particle interaction in packings of monodisperse angular particles. *Powder Technology*, *395*, 133–148.

Zhao, B., Wang, J., Andò, E., Viggiani, G., & Coop, M. R. (2020). Investigation of particle breakage under one-dimensional compression of sand using X-ray microtomography. *Canadian Geotechnical Journal*, *57*(5), 754–762.

Zhao, J., Zhao, S., & Luding, S. (2023). The role of particle shape in computational modelling of granular matter. *Nature Reviews Physics*, *5*(9), 505–525.

Zhao, S., & Zhou, X. (2017). Effects of particle asphericity on the macro-and micro-mechanical behaviors of granular assemblies. *Granular Matter*, *19*(2), 38.

Zheng, J., Ju, Y., & Wang, M. (2018). Pore-scale modeling of spontaneous imbibition behavior in a complex shale porous structure by pseudopotential lattice Boltzmann method. *Journal of Geophysical Research: Solid Earth*, *123*(11), 9586–9600.

Zheng, J., He, H., & Alimohammadi, H. (2021). Three-dimensional Wadell roundness for particle angularity characterization of granular soils. *Acta Geotechnica*, *16*(1), 133–149.

Zhong, H., Wang, Z., Zhang, Y., Suo, S., Hong, Y., Wang, L., & Gan, Y. (2024). Gas storage in geological formations: A comparative review on carbon dioxide and hydrogen storage. *Materials Today Sustainability*, *26*, 100720.

Zhou, B., & Wang, J. (2015). Random generation of natural sand assembly using micro X-ray tomography and spherical harmonics. *Géotechnique Letters*, *5*(1), 6–11.

Zhou, J., Lin, C., Chen, C., & Zhao, X. (2019). Reduction of groundwater buoyancy on the basement in weak-permeable/impervious foundations. *Advances in Civil Engineering*, *2019*, 7826513.

Zhou, W., Yang, L., Ma, G., Xu, K., Lai, Z., & Chang, X. (2017). DEM modeling of shear bands in crushable and irregularly shaped granular materials. *Granular Matter*, *19*(2), 25.

Zhou, Y., Zhou, B., Li, J., & Wang, H. (2016). Study on the multi-sphere method modeling the 3D particle morphology in DEM. *International Conference on Discrete Element Methods*, 601–608.

Zhu, W., Montesi, L. G., & Wong, T.-f. (1997). Shear-enhanced compaction and permeability reduction: Triaxial extension tests on porous sandstone. *Mechanics of Materials*, *25*(3), 199–214.

Zhu, W., & Wong, T.-f. (1999). Network modeling of the evolution of permeability and dilatancy in compact rock. *Journal of Geophysical Research: Solid Earth*, *104*(B2), 2963–2971.

Zimmerman, R. W., & Bodvarsson, G. S. (1996). Hydraulic conductivity of rock fractures. *Transport in porous media*, *23*(1), 1–30.

Zingg, T. (1935). Beitrag zur schotteranalyse. *Schweizer Mineralogische Petrographologische Mitteilungen*, *15*, 52–56.